3

Aerothermodynamic Design Problems of Winged Re-Entry Vehicles

In this chapter, we consider selected aerothermodynamic design problems of winged re-entry vehicles (RV-W's, Section 1.1). Of these vehicles the Space Shuttle Orbiter so far is the only operational vehicle. The other ones are conceptual studies or projects, which have reached different degrees of maturity.

RV-W's are either launched vertically with the help of rockets or, in the case of TSTO systems, horizontally from a carrier vehicle, the lower stage of the system. Other launch modes have been considered, viz., horizontal launch from a sled. Return to the Earth surface in any case is made with an unpowered gliding flight, followed by the horizontal landing on a runway.

A winged re-entry vehicle is heavier and more complex than a non-winged vehicle (capsule), Chapter 5, and in principle is a re-usable vehicle, unlike the latter. Its relatively high lift-to-drag ratio allows for a large cross-range capability. The aerodynamic design of RV-W's is driven by their wide Mach number and altitude range, whereas the structural design is driven by the large thermal loads, which are present on the atmospheric high-speed segment of the re-entry trajectory.

In this chapter we give an overview of aerothermodynamic phenomena found on RV-W's, look at a major simulation problem, viz., that due to high Mach number and enthalpy effects, and discuss particular aerothermodynamic trends. This is followed by a presentation of aerodynamic coefficients of the longitudinal motion of several vehicles. Finally, we study implications of Oswatitsch's Mach number independence principle in view of the hypersonic pitching moment anomaly observed during the first re-entry flight of the Space Shuttle Orbiter.

3.1 Overview of Aerothermodynamic Issues of Winged Re-Entry Vehicles

3.1.1 Aerothermodynamic Phenomena

Winged re-entry vehicles basically fly a braking mission during return from orbit or sub-orbit to the surface of Earth. They are, therefore, on purpose blunt and compact vehicles. The largest part of their trajectory is flown at high angle of attack, Fig. 3.1, which is in contrast to airbreathing cruise and acceler-

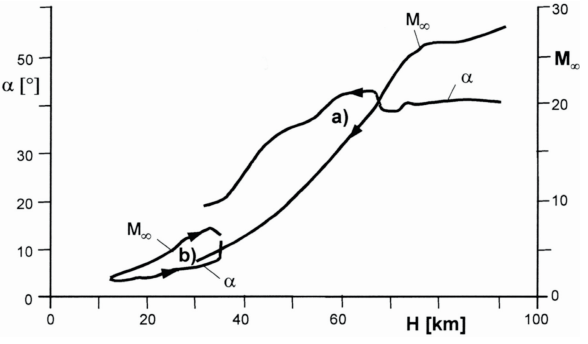

Fig. 3.1. Angle of attack α and flight Mach number M_∞ of a) the Space Shuttle Orbiter, and b) the TSTO space transportation system SÄNGER up to stage separation as function of altitude [1].

ation vehicles (CAV's, Chapter 4) and RV-NW's (Chapter 5). The high angle of attack of the vehicle with a relatively flat windward side (Sub-Section 3.2.2) increases the effective bluntness and thus increases further the (wave) drag of the vehicle. The large nose and wing leading edge radii, and the highly swept wing, permit effective surface radiation cooling [1].

The very small aspect ratios of such vehicles, as for all hypersonic flight vehicles, causes difficulties in low-speed control, such as during approach and landing. A remedy is to provide a double-delta, or strake-delta wing, Fig. 3.2.[1] In the case of HERMES, low-speed handling is improved by the winglets, see also Chapter 6.

In the aerothermodynamic design of RV-W's, flow and high temperature real gas phenomena which do not occur in subsonic, transonic and low supersonic flight must be taken into account. Major phenomena of the flow past RV-W's in the continuum-flow regime (below approximately 90–100 km altitude) are indicated in Fig. 3.3.

As mentioned, high drag demand and thermal load minimization call for a blunt nose and large angle of attack of the more or less flat lower side of the vehicle. Such a geometry gives rise to a detached bow shock and strong compressibility effects on the windward side. Due to the high angles of attack on the re-entry trajectory down to low altitudes, the flow past the windward side of the vehicle is of major interest. The leeward side is in the hypersonic shadow and is important in view of vehicle control, Section 2.1 and Chapter 6.

On the windward side of the vehicle, we first point out the presence of the entropy layer. Two forms of the entropy layer are possible [1]. One, typical for symmetric flow, has a (inviscid) velocity profile normal to the body surface which resembles the velocity profile of a slip-flow boundary layer. The second

[1] The effective wing surface includes the whole lower side of the airframe. With CAV's, the lower side of the airframe is also part of the propulsion system, Chapter 4.

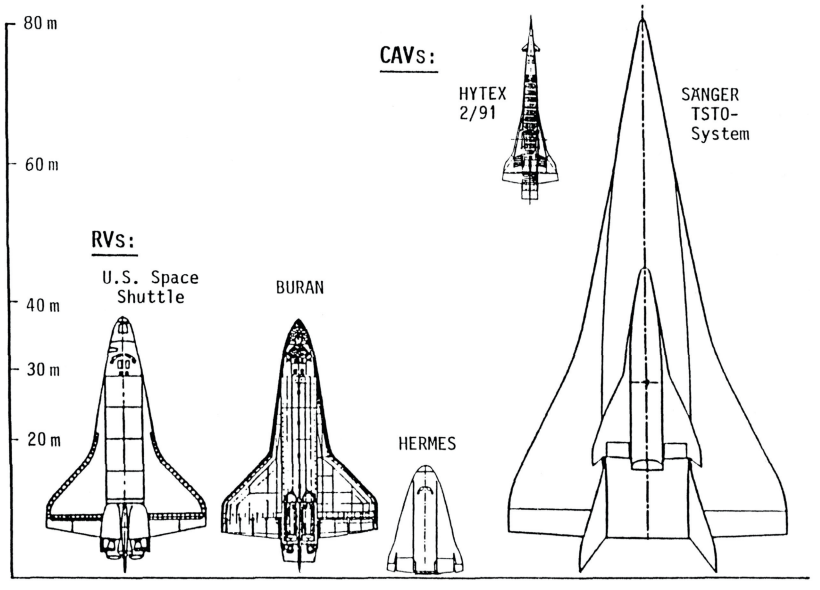

Fig. 3.2. Planform and size of example hypersonic flight vehicles [2]. HYTEX: air-breathing experimental vehicle studied in the German Hypersonics Technology Programme [3].

form is typical for asymmetric flow, where the streamline impinging the forward stagnation point does not cross the normal portion of the bow shock surface. In this case, the maximum entropy streamline lies off the body surface. It is also the minimum inviscid velocity streamline. The entropy layer hence has a wake-like structure. This form, which in general seems to be present at the windward side of a RV-W configuration at high angle of attack, is discussed in some detail in Sub-Section 6.2.2.

The windward side is marked further by strong high temperature real gas effects. Thermo-chemical equilibrium and non-equilibrium flow is present at the forward stagnation point region and downstream, depending on flight speed and altitude. The strength of surface catalytic recombination depends much on the properties of the surface coating. As indicated in Fig. 3.3, the general trend is that oxygen tends to recombine at rearward locations because the temperature is too high at forward locations where nitrogen may recombine.

The static temperature at the edge of the boundary layer is very large. The attached viscous flow is in general of second-order boundary layer type [1]. Above 40–60 km altitude, the boundary layer is usually laminar, which eases some of the aerothermodynamic simulation problems. Below that altitude, the boundary layer becomes turbulent. The wall temperature, due to surface radiation cooling, is much smaller than the recovery temperature, decreasing at

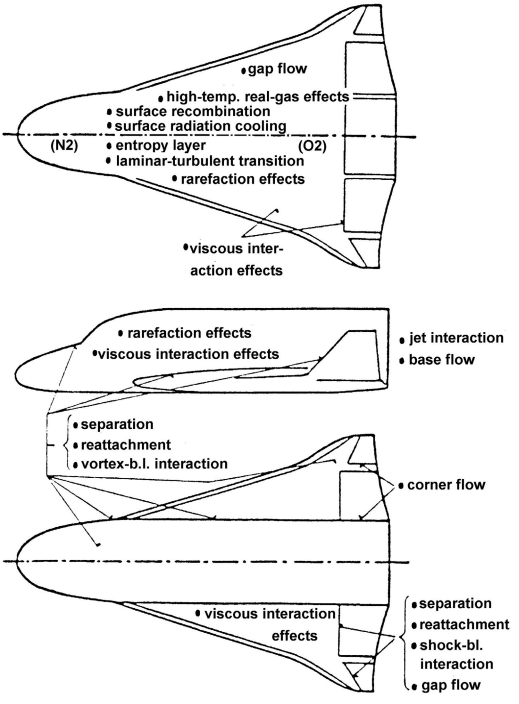

Fig. 3.3. Locations of flow and high temperature real gas phenomena on a RV-W (HERMES) at hypersonic flight [4]. Upper figure: view from below, middle figure: side view, lower figure: view from above. (N2), (O2): location of possible/expected catalytic surface recombination of nitrogen, oxygen. Note that all indicated phenomena depend on flight speed and altitude, and on the shape and attitude of the given RV-W.

$M_\infty = 24$ and 70 km altitude from around 2,000 K at the stagnation point to around 1,000 K at a downstream distance of about 30 m.

The radiation-adiabatic temperature T_{ra}, also called radiation equilibrium temperature, in general is a good approximation of the actual wall temperature T_w. The heat flux q_w into the thermal protection system (TPS) is small, compared to the heat flux in the gas at the wall, q_{gw}, Section 9.1. Due to the large temperature and heat flux gradients downstream from the nose, partly also in lateral direction, the thickness of the TPS varies with the location in order to reduce its mass. It can be noted that the TPS of the Space Shuttle Orbiter has about 30,000 tiles of different thickness, shape and size.

Due to the large angle of attack, the boundary layer edge Mach number M_e at the vehicle's windward side is small compared to the flight Mach number.[2] Hence the boundary layer is transonic/supersonic in nature. When the

[2] Of influence are also the large static temperature at the windward side and high temperature real gas effects.

boundary layer becomes turbulent at the lower segments of the trajectory, both temperature and heat flux at the wall increase markedly, Section 9.2. Hence thermal loads are also of concern in that portion of the trajectory.

Hypersonic viscous interaction and rarefaction effects are mainly confined to the initial re-entry trajectory segment. Strong interaction phenomena, like separation, attachment, reattachment, shock/boundary layer as well as vortex/boundary layer interaction may occur at several locations, depending on the shape and attitude of the flight vehicle, but especially in the hinge-line neighborhood of aerodynamic control surfaces, Section 6.3. Jet/boundary layer interaction occurs at the location of the thrusters of the reaction control system, Section 6.5. Base flow and base drag in general are of minor interest on the high-speed segments of the trajectory, because the base pressure is close to zero there.

Summarizing, we note that we have mainly in the flow path at the windward side of RV-W's:

- strong compressibility effects,
- strong high temperature real gas effects,
- surface radiation cooling, mostly without but partly with non-convex effects, radiation cooling related hot-spot situations,
- complex surface heat transfer mechanisms (thermal surface radiation, non-equilibrium effects, catalytic surface recombination, slip flow and temperature-jump),
- strong shock/shock and shock/boundary layer interaction, corner flow, boundary layer separation,
- viscous and thermo-chemical surface effects,
- hypersonic viscous interaction and rarefaction effects at high altitudes,
- gap flow (trim and control surfaces, thermal protection system),
- strong flow interactions related to reaction control systems,
- base flow, plume spreading,
- laminar flow at altitudes above approximately 40–60 km,
- Mach number and surface property effects on laminar–turbulent transition and on turbulent flow phenomena.

It is important to note, and this holds for the aerothermodynamic phenomena of CAV's, ARV's and RV-NW's, that the listed phenomena usually do not occur in isolation. Strong interference may occur which can result in a highly nonlinear behavior. Such interference may make it difficult to understand each effect and its influence on flight vehicle performance. In such situations, properly simulating the effects in ground simulation facilities or computationally is very difficult, if not impossible.

3.1.2 Major Simulation Problem: High Mach Number and Total Enthalpy Effects

In view of the dominating compressibility effects, Mach number and high temperature real gas effects are extremely important, but difficult to treat in ground-simulation, Section 9.3, see also the discussions in [1]. This holds for both ground facility and computational simulation.

In principle, ground simulation in modern facilities is possible for the whole Mach number range of RV-W's. The problem is to have a sufficiently large wind-tunnel or shock-tunnel model and further, regarding especially data set generation, a high enough productivity of the ground-facility (polars per time unit). The latter holds for computational simulation, too. However, the growing computer capabilities will help to overcome this problem rather soon.

The fact that force coefficients, shock wave shapes, etc. become independent of the flight Mach number above a configuration-dependent Mach number (Oswatitsch's Mach number independence principle, Sub-Section 3.6.1), allows measurements to be made at much lower Mach numbers than actual flight Mach numbers. Despite this there are dangers, as was seen with the hypersonic pitching moment anomaly observed with the Space Shuttle Orbiter, Section 3.5.

High-enthalpy facilities allow real flight enthalpies to be achieved but at too low a Mach number due to the high static temperature in the test section. However, if the Mach number is large enough, so that independence is present, this is not a major problem.[3] The problem is the role of high temperature real gas effects on the Mach number independence principle. We discuss this problem in Section 3.6.

In view of the still growing computation capabilities, one is tempted to assume that data generation in ground simulation facilities will become obsolete in some years. This assumption requires that flow physics, thermodynamics and surface property models are improved in computational simulation.

3.2 Particular Trends in RV-W Aerothermodynamics

3.2.1 Stagnation Pressure

The stagnation pressure coefficient for incompressible flow is with $p_{stag} = p_\infty + q_\infty$ where the dynamic pressure $q_\infty \equiv \rho_\infty v_\infty^2/2$:

$$c_{p_{stag}} \equiv \frac{p_{stag} - p_\infty}{q_\infty} = 1. \tag{3.1}$$

At the stagnation point in subsonic flow, isentropic compression yields $p_{stag} \equiv p_t$ [1] and hence

[3] Of course, there are other problems in such facilities, which are discussed in [1].

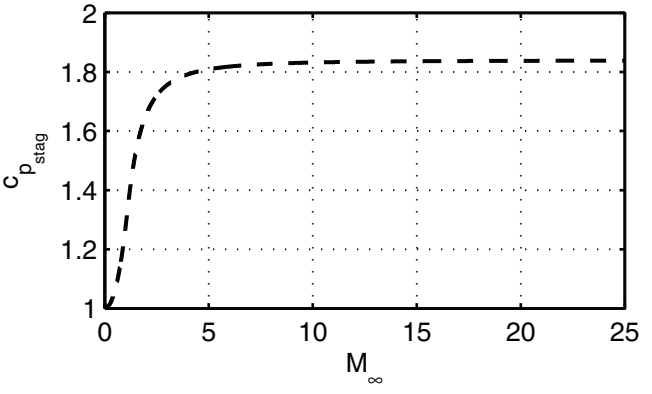

Fig. 3.4. Stagnation pressure coefficient $c_{p_{stag}}$ as function of the flight Mach number M_∞, $\gamma = 1.4$.

$$c_{p_{stag}} = \frac{2}{\gamma M_\infty^2}\left[\left(1+\frac{\gamma-1}{2}M_\infty^2\right)^{\gamma/(\gamma-1)} - 1\right]. \tag{3.2}$$

This means that for $0 < M_\infty \leqq 1$ and $\gamma = 1.4$ we have $1 \leqq c_{p_{stag}} \leqq 1.2756$.

In supersonic flow, a bow shock exists in front of a blunt body which causes a loss of total pressure. In the case of a symmetric blunt body at zero angle of attack, the total pressure loss can be treated as that across the normal shock portion of the bow shock, see, e.g., [1]. Taking that into account, we have:

$$c_{p_{stag}} = c_{p_{t_2}} = \frac{2}{\gamma M_\infty^2}\left\{\left[\frac{(\gamma+1)^2 M_\infty^2}{4\gamma M_\infty^2 - 2(\gamma-1)}\right]^{\gamma/(\gamma-1)}\left[\frac{2\gamma M_\infty^2 - (\gamma-1)}{\gamma+1}\right] - 1\right\}. \tag{3.3}$$

For very large Mach numbers where $M_\infty \to \infty$, this relation reduces to:

$$c_{p_{stag}} = c_{p_{t_2}} \to \frac{4}{\gamma+1}\left[\frac{(\gamma+1)^2}{4\gamma}\right]^{\frac{\gamma}{(\gamma-1)}}. \tag{3.4}$$

With $\gamma = 1.4$, we obtain $c_{p_{stag}} = 1.8394$. Hence, in supersonic and hypersonic perfect gas flow with $M_\infty > 1$, $1.2756 < c_{p_{stag}} < 1.8394$, Fig. 3.4. This means that at hypersonic Mach numbers, a finite but not very large pressure coefficient exists at the forward stagnation point of a blunt body.

However, the question is, how do high temperature real gas effects change this picture. Table 3.1 lists a number of computed cases for which the stagnation pressure coefficients as a function of the Mach number are shown in Fig. 3.5. In Fig. 3.5 the stagnation pressure coefficients, actually the c_{p_w} at the forward stagnation points, of the computations are marked by symbols. In addition, curves of $c_{p_{stag}}(M_\infty)$ are given which were found with the normal-shock relations with different values of γ_{eff}, Sub-Section 10.1.3. These curves represent the stagnation pressure coefficient $c_{p_{t_2}}$ just behind the normal shock.

Table 3.1. Configuration, flight data and computation details of the stagnation pressure data given in Fig. 3.5. For Nos. 6 and 7, mean values from several contributions to [5] (proceedings of the 1991 Antibes workshop) are given in Fig. 3.5.

No.	Configuration	M_∞ [−]	H [km]	α [°]	Eqs.	Gas Model	Ref.	Remarks
1	double ellipse	6.6	–	0	NS	non-eq.	[5]	WT cond.
2	sphere	10	30.0	0	Euler	eq.	[6]	
3	sphere	15	50.0	0	Euler	eq.	[6]	
4	sphere	20	50.0	0	Euler	eq.	[6]	
5	Space Shuttle Orb.	23.86	73.1	40	NS	non-eq.	[7]	flight cond.
6	double ellipsoid	25	75.0	40	Euler, NS	non-eq.	[5]	
7	double ellipsoid	25	75.0	40	Euler, NS	eq.	[5]	

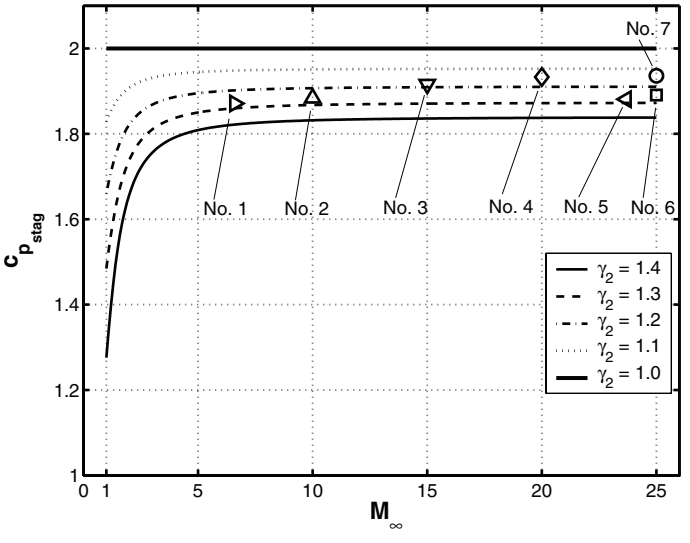

Fig. 3.5. Computed stagnation pressure coefficient $c_{p_{stag}}$ of different, mainly inviscid cases, Table 3.1, as function of the flight Mach number M_∞. Included are curves $c_{p_{stag}}(M_\infty)$ for different γ_{eff} ($\equiv \gamma_2$).

In reality, γ is not constant in the layer between the bow shock and the body surface. Further, if the body is asymmetric or at angle of attack, the streamline impinging the forward stagnation point does not cross the normal portion of the bow shock surface. In this case, the maximum entropy streamline lies off the

body surface. Nevertheless, the curves in Fig. 3.5 give the general trend of c_{p_w} in terms of $c_{p_{stag}}$ at the forward stagnation point of blunt bodies at hypersonic flight Mach numbers. For $\gamma \to 1$, $c_{p_{stag}} = 2$ at all Mach numbers which, of course, represents the Newton limit ($M_\infty \to \infty$) [1].

We note that $c_{p_{stag}}$ increases with increasing Mach number M_∞ for all γ_{eff}. The gradient $d\,c_{p_{stag}}/d\,M_\infty$ becomes small and then approximately zero, Figs. 3.4 and 3.5. Decreasing γ_{eff} increases $c_{p_{stag}}$ at all Mach numbers. As we will see in Section 3.6, this behavior is reversed, at least for blunt body shapes, at some location downstream of the stagnation point region. The crossover location in general lies at the beginning of the flat surface portion of the windward side, see also next sub-section. Behind it, the inviscid wall pressure coefficient c_{p_w} decreases with increasing Mach number as well as with decreasing γ_{eff}, both independently of each other. However, there exists presumably—for sufficiently high flight Mach numbers—a wall (boundary-layer edge) Mach number interval, the "benign" M_w interval, where these effects are so small that we have virtually attained flight Mach number and real gas effect independence.[4]

Also important is the observation that the small gradient $d\,c_{p_{stag}}/d\,M_\infty$ at high supersonic/hypersonic Mach numbers would make flight speed and Mach number determination with a conventional Pitot tube, for instance during reentry of a RV-W-type vehicle, difficult if not impossible at high Mach numbers. This effect is also a consequence of Oswatitsch's Mach number independence principle.

There are possible situations in a vehicle where a much larger wall pressure than the forward stagnation point pressure can arise. This happens when a multiple shock system is present, which leads, for instance, to the Edney type IV shock/shock interaction [1]. At such locations, a localized, intense wall pressure of ten times and more than the stagnation pressure can exist. Unfortunately in such strong interaction situations, the thermal loads are also locally very large. We can find such a situation at locations where the vehicle bow shock interacts with an embedded bow shock, for instance, that of a pylon in the famous X-15 case which was the motivation for Edney's work [8]. Other locations where such situations can arise are at wings, stabilizers if the sweep angle locally is small or in the inlets of CAV's and ARV's.

3.2.2 Topology of the Windward Side Velocity Field

From an aerothermodynamic point of view, the windward side of a RV-W ideally should be predominantly flat. This also means that fuselage and wing combined should have a plane lower side. A flat windward side would lead to a larger bow shock portion with high shock angle θ against the free-stream. In

[4] The curves in Fig. 3.5 suggest Mach number independence occurs at lower Mach numbers with increasing high temperature real gas effects. However, such a conclusion should be drawn with caution.

Table 3.2. Flight parameters of the numerical simulation of the flow past the HALIS configuration [9].

Case	M_∞	H [km]	α	ρ_∞ [kg/m^3]	T_∞ [K]	v_∞ [m/s]	T_w [K]	η_{bf}
F4 conditions	8.86	-	40°	$0.545{\cdot}10^{-3}$	795.0	4,930.0	300.0	15°
Flight conditions	24	70.0	40°	$0.55{\cdot}10^{-4}$	212.65	7,028.0	1,300.0	15°

this way, the wave drag can be enhanced and the total drag maximized. We find such lower side shapes on most of the flight vehicles considered in Section 3.3.

A flat or approximately flat windward side leads to a more or less two-dimensional flow field. This has the advantage of an optimal or near-optimal onset flow geometry of the body flap and also of other trim and control surfaces, Section 6.2. See also Figs. 6.3 and 6.4.

If the windward side of a RV-W is sufficiently flat, we have another large advantage, viz., that in a large angle of attack domain, the flow there is flight Mach number and high temperature real gas effects independent, Section 3.6. As discussed in that section, such independence is lost if boattailing is present, especially real gas independence. This is the cause of the hypersonic pitching moment anomaly experienced during the first flight of the Space Shuttle Orbiter.

Last, but not least, another interesting advantage of the full or approximately two-dimensionality of the flow is, that flow field studies, both inviscid and viscous, can be made with the help of plane or axisymmetric two-dimensional equivalent shapes of the original configuration, Sub-Section 10.1.1 and also Section 3.6.

Because the (blunt) wing leading edges of RV-W's are strongly swept, the vehicle planform and hence the windward side in many cases resembles more or less the lower side of a delta wing, or double-delta wing, see, e.g., Figs. 3.2 and 3.3. On such shapes, we find the desired topology of the surface velocity/skin-friction field: downstream of the nose area, we have on the flat portion a relatively two-dimensional, planar flow between two primary attachment lines.

In reality, the windward sides of RV-W's are only approximately flat and, even that, not necessarily everywhere. Take for instance the Space Shuttle Orbiter, Figs. 3.40 and 3.41. Large portions of its windward side are approximately flat for $x/L \gtrapprox 0.25$. Ahead of this location, the fuselage resembles that of a blunt cone. Such geometric variations are reflected by the skin friction lines, such as those computed for HALIS, Fig. 3.6. The computations for this figure and Fig. 3.7 were made in the frame of the the Manned Space Transportation Programme (MSTP) for the conditions of the ONERA tunnel F4 and flight conditions with the parameters given in Table 3.2.

For the example shown in Fig. 3.6, the forward stagnation point is located at the lower side of the configuration at $x \approx 0.4$ m, compare with Fig. 6.5 in Sub-Section 6.2.2. Up to $x/L \approx 0.25$, we have an attachment line at the

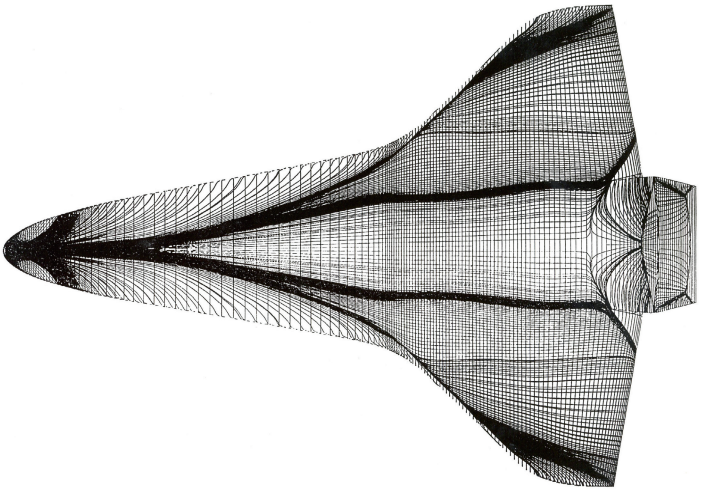

Fig. 3.6. HALIS flow field computation, flight conditions, Table 3.2: skin-friction lines on the windward side. Laminar Navier–Stokes solution with chemical non-equilibrium, [10].

lower symmetry line (blunt cone flow).[5] Downstream of this location, the central attachment line branches into the left and right attachment line. They are located below the strake (first delta of the wing) and then, at the second delta, below and close to the leading edge. We see that between the two attachment lines, the flow is indeed approximately two-dimensional, with larger deviations at the outer part of the second delta due to its dihedral, Fig. 3.41.

The above pattern is basically also seen in Fig. 3.7. We have included this figure because it shows several other interesting features of the skin friction topology. First, we see differences in the skin friction pattern compared to that in Fig. 3.6. Although the flight cases are the same, the two-dimensionality is now less pronounced. The separation region ahead of the deflected body flap is considerably larger in Fig. 3.6.

In Fig. 3.7, the influence of wall temperature on the extent of the separation region can be clearly seen. In the F4 case (upper part), the temperature is much lower than in the flight case (lower part).[6] Consequently, the boundary layer has a higher flow momentum and can better negotiate the pressure

[5] Note that in this figure, in contrast to Fig. 3.7, the skin-friction lines were computed from the aft part of the configuration towards the forward stagnation point. This gives a richer pattern, however, partly with a somewhat undesirable accumulation of skin-friction lines.

[6] The assumed constant wall temperature $T_w = 1{,}300$ K in the flight case is not a good approximation of the real wall temperature. That is better approximated by the radiation-adiabatic temperature of approximately 1,000 K, which is at the position of the hinge line of the body flap. The fact, that hypersonic vehicles

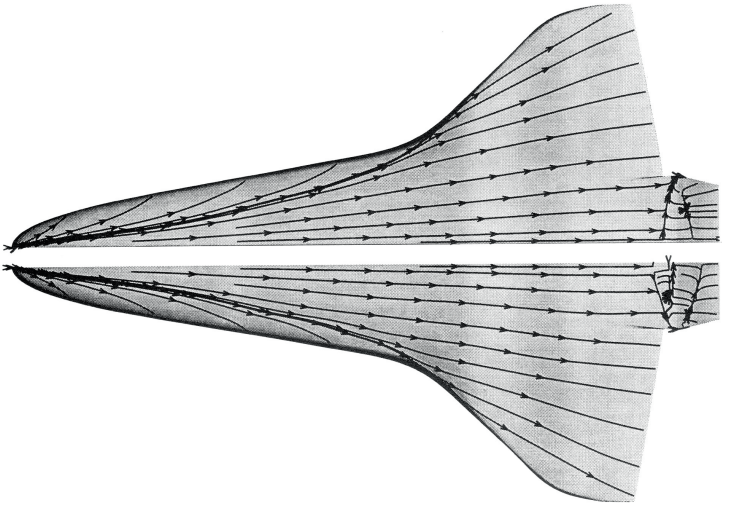

Fig. 3.7. HALIS flow field computation, upper part F4 conditions, lower part flight conditions, Table 3.2: skin-friction lines on the windward side. Laminar Navier–Stokes solutions with chemical non-equilibrium [9].

increase at the flap, see also Fig. 6.8. The differences in the skin-friction line patterns in Figs. 3.6 and 3.7 are possibly due to different grid structures and grid resolutions. This is not the case for the two patterns shown in Fig. 3.7. The differences between the F4 case (upper part) and the flight case (lower part) are small, except for the vicinity of the body flap and at locations where the flow is more three-dimensional. A larger wall temperature in any case enhances a given three-dimensionality of a boundary layer [1].

What we basically see from the above is an illustration of the Mach number independence principle, Section 3.6. The F4 as an high-enthalpy ground facility, with total enthalpy that is lower than actual flight. As is typical, F4 has a high free-stream temperature and low free-stream Mach number. Nevertheless, the Mach number appears to be large enough so that Mach number independence is more or less reached. Mainly, therefore, we see only small differences in the skin-friction line patterns.

A drastically different skin-friction line pattern is present on the windward side of the Blunt Delta Wing (BDW), Fig. 3.8 [11]. The pattern resembles that usually found on the windward side of true delta wings. The BDW was derived as a simple generic configuration for aerothermodynamic studies in the research activities of the HERMES project [12].

Figure 3.8 shows the forward stagnation point and the two primary attachment lines, which all lie at the large angle of attack at the lower side of the

have radiation cooled surfaces was not yet fully accepted by the aerothermodynamic community at the time of the computations.

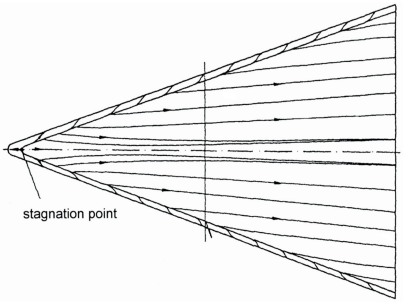

Fig. 3.8. Skin-friction lines on the windward side of the Blunt Delta Wing (BDW) [11]. Navier–Stokes solution, laminar flow, perfect gas, $M_\infty = 7.15$, $H = 30$ km, $L_{BDW} = 10$ m, $\alpha = 15^\circ$.

vehicle. The lower side of the BDW has a rather large dihedral angle of 15°. Despite the strong dihedral, we see a relatively two-dimensional pattern of skin friction lines between the primary attachment lines. For a detailed discussion of the topology of the flow field past the BDW, see [1].

We note finally, that the lee side of a RV-W at hypersonic speed and large angle of attack does not contribute much to the aerodynamic forces acting on the vehicle, Sub-Section 3.2.3. The lee side pressure depends on the flight Mach number, altitude and angle of attack. For the BDW, with the flight parameters given in Fig. 3.8, the computed wall pressure coefficient at $x/L = 0.5$ is $c_{p_w} = 0.24$–0.32 on the windward side and $c_{p_w} = -0.022$ to -0.025 on the lee side [11].[7]

This relative lack of influence of the lee side on the aerodynamics is also reflected by the thermal loads on vehicle surface. The wall temperature $T_w = T_{ra}$ and the heat flux in the gas at the wall q_{gw} are significantly lower on the lee side than on the windward side. Because temperature and heat flux are so low at the lee side, this side usually does not need a coating with a high surface emissivity. The lee side of RV-W such as the Space Shuttle Orbiter actually have white surfaces. In orbit, the vehicle turns this side towards the Sun. The low emissivity prevents heating of the vehicle due to radiation from the Sun. However, it can be noted that RV-W's may have on the lee side or along the fuselage sides hot and cold spots vortex interaction phenomena [11], see also the discussion in Section 3.3 of [1]. Finally, in contrast to RV-W's, CAV's and ARV's need surfaces with high emissivity all around because they fly at very low angles of attack, the latter type only at ascent.

3.2.3 Lift Generation

Another trend, typical for high supersonic and hypersonic flight, is that with increasing flight Mach number, the leeward side of a wing ceases to contribute

[7] From eq. (3.6), the vacuum pressure coefficient, in this case is $c_{p_{vac}} = -0.028$.

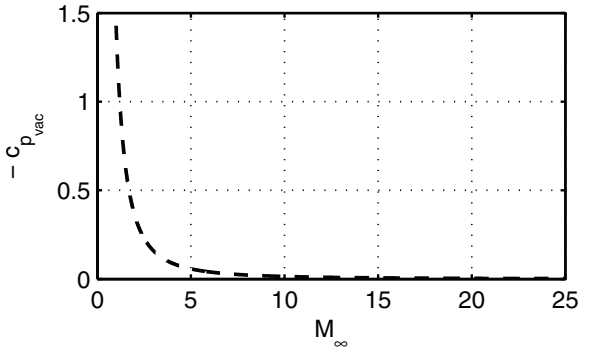

Fig. 3.9. Vacuum pressure coefficient $c_{p_{vac}}$ as function of the flight Mach number M_∞, $\gamma = 1.4$.

to lift. This is due to the limited Prandtl–Meyer expansion angle for supersonic flows [1]. The pressure coefficient can be written as

$$c_p \equiv \frac{p - p_\infty}{q_\infty} = \frac{2}{\gamma\, M_\infty^2} \left(\frac{p}{p_\infty} - 1 \right). \tag{3.5}$$

If we define the expansion limit by $p \to 0$, we obtain the so-called vacuum pressure coefficient as a function of Mach number:

$$c_{p_{vac}} = -\frac{2}{\gamma\, M_\infty^2}. \tag{3.6}$$

Figure 3.9 shows the rapid decrease of the vacuum pressure coefficient with increasing Mach number. This coefficient essentially reaches zero at $M_\infty \approx 10$ and thereafter is Mach number independent. For practical purposes, usually the value $c_{p_{min}} = 0.8 c_{p_{vac}}$ is taken. At large Mach numbers, the required expansion turning angles to reach $c_{p_{min}}$ are small and this has a bearing on CAV design.

Prandtl–Meyer theory does not allow the zero pressure state to be determined. This state can be obtained by equating the total enthalpy of the flow to the kinetic energy, assuming that the internal energy tends to zero [1]. For a perfect gas, have $V_{max} = \sqrt{2\, c_p\, T_t}$ at $T = 0$, and hence $p = 0$. Applying thin airfoil theory [13], the pressure coefficient on the upper, lee side of a flat plate, being at a negative inclination of $\overline{\alpha}$ is given by

$$c_p = \frac{2\,\overline{\alpha}}{\sqrt{M_\infty^2 - 1}}. \tag{3.7}$$

Equating this to eq. (3.6) yields:

$$\overline{\alpha}_{vac} = -\frac{\sqrt{M_\infty^2 - 1}}{\gamma M_\infty^2}. \tag{3.8}$$

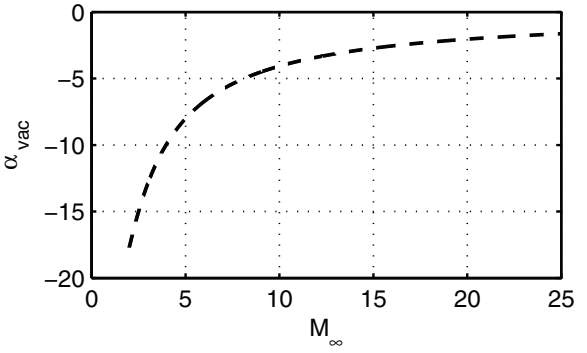

Fig. 3.10. Inclination angle α_{vac} ($\equiv \overline{\alpha}_{vac}$) needed to reach the vacuum pressure coefficient $c_{p_{vac}}$ as function of the flight Mach number M_∞, $\gamma = 1.4$.

This relationship, plotted in Fig. 3.10, shows that small negative values of $\overline{\alpha}$ suffice to reach $c_{p_{vac}}$. An approximate application of thin airfoil theory can be made by taking into account the bow shock caused by a blunt nose or blunt leading edge. A local Mach number instead of M_∞ is then used for obtaining the pressure coefficient. Remember in this context the very different flow situations at RV-W's and CAV/ARV's [1].

The vanishing pressure at the lee side of a configuration at high Mach numbers is called the hypersonic shadow effect. This phenomenon permits the use of so-called impact methods, especially the Newton method, in design work, because the lee side flow does not play a role. Further, due to this phenomenon, the HALIS configuration, [14], see below, as a simplified Space Shuttle Orbiter configuration and also other similar configurations—at sufficiently large angle of attack—can be used for numerical investigations.

3.2.4 Base Pressure and Drag

Directly related to the expansion is the base pressure. At the vehicle's base, the flow turns up to 90° and hence $c_{p_{vac}}$ is reached. Therefore, the base pressure is extremely low and base drag is high. RV-W's thus far have blunt afterbodies for locating the propulsion system or for connection to the launch vehicle, see the images given in Section 3.3. The blunt afterbody drag does not pose a problem, because a large drag is desired on most of the re-entry trajectory. On the low Mach number part of the trajectory, especially in the transonic regime, the reduction of L/D usually is tolerated. The situation is different for CAV/ARV's,

Sub-Section 4.2.4. For these classes of vehicles, the base drag, especially in the transonic flight regime, is a major problem.[8]

Blunt wing/flap trailing edges are usually employed on RV-W's to alleviate the large thermal loads there. These blunt trailing surfaces can have an interesting side effect. During the development of the X-15, it was seen that very large, all-movable[9] horizontal and vertical stabilizer surfaces were needed to assure directional and pitch stability [15]. To reduce the vertical stabilizer surface, the design was changed from the original thin airfoil to a wedge design, which was proposed in [16]. The 10° wedge, leading to considerable trailing-edge bluntness, improved the effectiveness of the stabilizer surface and yielded a smaller size. The improvement is due to the initial load on both sides of the wedge surface, and the fact that larger setting angles are possible before the vacuum limit is reached on the respective lee side. It seems, however, that no further consideration of the proposal of [16] was made later for RV-W's.

3.3 Aerodynamic Performance Data of RV-W's

In this section, we give summaries from aerodynamic data sets of longitudinal motion of some RV-W's which were established in recent decades. Two of these vehicles, which were never built, are the European HERMES and the Japanese HOPE-X. Three are demonstrators, viz., the American X-38[10] and X-34, and the German PHOENIX. These were manufactured and have conducted at least some drop tests. Finally, there is the Orbiter of the Space Shuttle system, which is the only truly operational RV-W. In Table 3.3 we list some geometrical data of the configurations in chronological order.

In the following sub-sections, we discuss selected aerodynamic coefficients of these configurations which are available from our own industrial design work and the literature. We consider in general the untrimmed state, i.e., the data found, for instance, in a ground-simulation facility. The pitching moment in all cases, except for the X-38, is given with all aerodynamic control surfaces in the neutral position ($\eta_{body\ flap\ and\ elevons} = 0°$).

In general the lift-to-drag ratio in the trimmed state is smaller than in the untrimmed state, regardless of whether the vehicle flies stably or not, Sub-Section 3.4.2. In the unstable case, which is characterized by downward deflected trim surfaces, the resulting aerodynamic force $\underline{F}_{aero,trim}$ is larger than the aerodynamic force in the untrimmed state $\underline{F}_{aero}$, Fig. 3.34. For the stable case, it is the other way around. The pitching moment charts are given for

[8] We note in this context the tail cone which is attached to the Space Shuttle Orbiter for ferry flights on top of the Boeing 747 Shuttle Carrier Aircraft. It reduces drag and buffeting due to flow separation.

[9] All-movable stabilizer surfaces have the benefit that no extra control surfaces are employed and hence the strong interaction phenomena around the hinge lines are avoided, Chapter 6.

[10] The X-38 is only approximately a RV-W, Sub-Section 3.3.5.

Table 3.3. Geometrical data of the considered RV-W's.

Vehicle	L_{ref} [m]	A_{ref} [m^2]	Wing span [m]	Sweep angle [°]	Strake angle [°]	x_{cog}/L_{ref} [–]
Space Shuttle Orbiter	32.774	249.91	23.790	45.0	81.0	0.650
HERMES	15.500	73.000	9.375	74.0	–	0.600
HOPE-X	15.249	50.220	9.670	55.0	75.0	0.635
X-34	17.678	33.213	8.534	45.0	80.0	0.600
X-38	8.410	21.670	3.658	–	–	0.570
HOPPER	43.650	545.120	27.200	55.0	–	0.680
PHOENIX	6.900	15.14	3.84	62.5	–	0.700

provisionally chosen center-of-gravity positions x_{cog}/L_{ref} locations listed in Table 3.3, which are not necessarily the actual positions. Therefore, they may not reflect the state of trim and stability of the vehicle.

3.3.1 Space Shuttle Orbiter

The Space Shuttle system consists of three elements:

- two solid rocket boosters,
- external tank,
- Orbiter vehicle.

The Space Shuttle is a semi-reusable system of which the burned-out boosters are recovered from the Atlantic Ocean, refurbished and then refilled with solid propellant. The external tank is expended. The Orbiter is reused after inspection and refurbishment. This system is the only winged and manned system to reach orbit and to land horizontally. So far, the fleet has performed more than 120 flights.

The missions of the Space Shuttle involve carrying large and heavy payloads to various orbits including elements of the International Space Station (ISS), performing service missions, also to satellites, e.g. Hubble, and serving as a crew transport system for the ISS.

The Space Shuttle program was officially started by the Nixon administration in January 1972. The first launch took place on April 12, 1981, followed by the first re-entry flight on April 14, 1981. Detailed accounts regarding flight experience, aerothermodynamic performance and problems of this flight were

published in, for instance, [17, 18]. Five Orbiter vehicles were built and flown (first flight):

– Columbia (1981),
– Challenger (1983),
– Discovery (1984),
– Atlantis (1985),
– Endeavour (1992).

Challenger (1986) and Columbia (2003) were lost by accidents. It is planned to retire the Space Shuttle system from service in 2010.

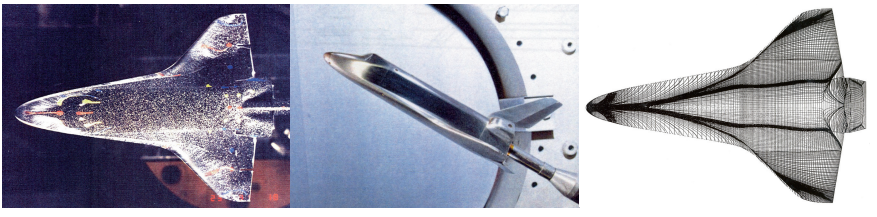

Fig. 3.11. Space Shuttle Orbiter: oil flow pattern on the leeward side of a wind tunnel model (left), model in wind tunnel (middle) [19], skin-friction lines on the windward side found with numerical flow simulation (right) [10].

We are concerned here with some aerodynamic data of the Orbiter vehicle, Fig. 3.11. The selected aerodynamic data, shown in Fig. 3.12, are taken from [20]. The lift coefficient behaves linearly up to $M = 1.5$, but shows a positive lift-curve break (change of the gradient $dC_L/d\alpha$ with α) at high Mach numbers. The drag coefficient has its minimum for all Mach numbers at small angles of attack, as expected, and rises then fast to large values. The drag coefficient in the transonic range is the largest. Mach number independence is present for $M_\infty \gtrapprox$ 5–10, although not directly visible due to data from selected Mach numbers being presented, see also Figs. 3.32 and 2.3.

The maximum lift-to-drag ratio $L/D|_{max} \approx 4.5$ in the subsonic regime and reduces to $L/D|_{max} \lessapprox 2$ in the hypersonic regime. This is somewhat lower than that of the HOPPER/PHOENIX and HOPE-X shapes, Figs. 3.29 and 3.18.

The behavior of the pitching moment with respect to the Mach number is very similar to that of HOPPER/PHOENIX shape, Fig. 3.29. The largest negative derivative $dC_m/d\alpha$, found at $M_\infty = 1.1$ indicates strong static stability for $\alpha \lessapprox 18°$. The configuration become unstable for $M_\infty \gtrapprox 3$, Fig. 3.12, lower right. For $\alpha \gtrapprox 20°$ we see a stable but untrimmed behavior. The forward part of the upper side of the configuration contributes no more to the nose-up moment because $c_{p_{vac}}$ is reached there.

Further one can observe for $0.8 \leqq M_\infty \leqq 1.5$ a sudden change of the derivative $dC_m/d\alpha$ from negative to positive at $\alpha \approx 20°$, indicating static instability

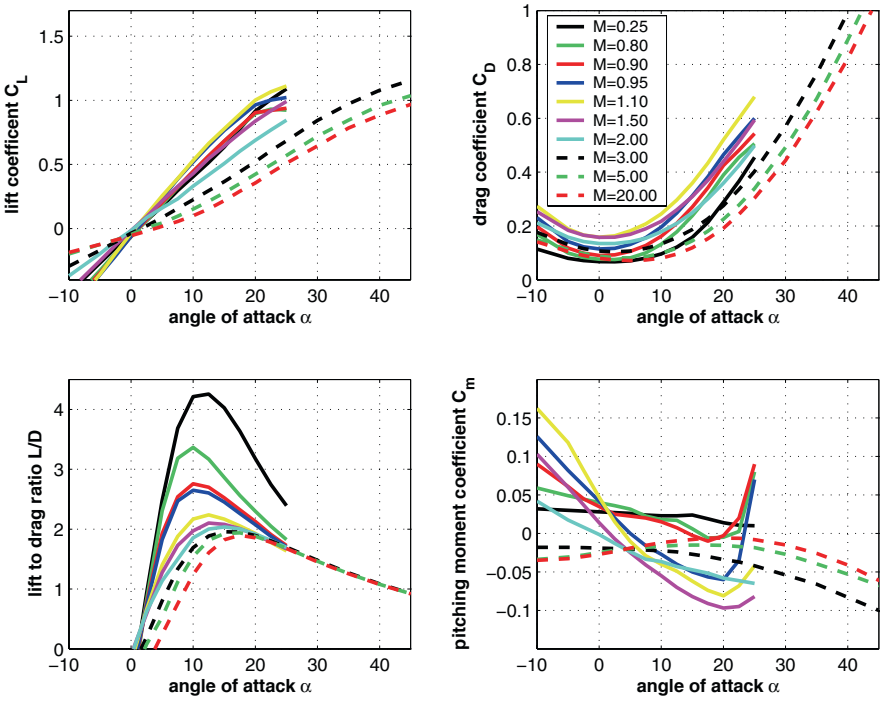

Fig. 3.12. Selected aerodynamic data of the Space Shuttle Orbiter for various subsonic to hypersonic Mach numbers as function of the angle of attack α; moment reference point $x_{ref} = 0.65\ L_{ref}$. Data source: [20].

there. This is the same for the HOPPER/PHOENIX shape and to some extent also for the HOPE-X shape, Fig. 3.18. The reason is the onset of leading edge vortex breakdown above the wing, travelling continuously forward with increasing α. There are no marks of this behavior in the HERMES aerodynamics since nonlinearity of the lift up to $\alpha < 30°$ cannot be detected for this shape, Fig. 3.14. Remember, however, that the Orbiter data are for the chosen $x_{cog}/L_{ref} = 0.65$. The actual longitudinal center-of-gravity[11] envelope of the Orbiter at the entry interface of 121.92 km (400 kft) altitude up to the year 1995 was $0.65 < x_{cog}/L_{ref} < 0.675$, however, during STS-1 it was $0.667 \lessapprox x_{cog}/L_{ref} \lessapprox 0.671$ [21].

[11] Note that in [21] and in other contributions to [18], the x-location of the center-of-gravity are given in terms of the design coordinate system. Its origin is 5.9944 m (236.0 in.) ahead of the nose point, which usually in aerodynamics lies at $x/L = 0$.

3.3.2 HERMES Configuration

In 1984, the French government launched a proposal for the development of a space transportation system in order to guarantee Europe an autonomous and manned access to space. Key parts of this system were the RV-W spaceplane HERMES, responsible for a gliding re-entry from space to an Earth landing site, Fig. 3.13, and the launch system ARIANE V, which at that time was a completely new rocket system. The original French project officially became a European project under the supervision of the European Space Agency (ESA) in November 1987. HERMES was conceived to have the following features:

- initially, the transportation of six astronauts and 4,500 kg payload into space, and after a later reorientation a reduction of the transport capacity to three astronauts and 3,000 kg payload,
- ascent to near Earth orbit (up to 800 km) on top of the ARIANE V rocket,
- 30–90 days mission duration,
- total launch mass 21,000 kg,
- full reusability.

In 1993 the HERMES project was cancelled due to the new political environment (end of the cold war) and budget constraints. No HERMES vehicle, nor the proposed sub-scale experimental vehicle MAIA [4], was ever built.

The aerodynamic data presented here for the subsonic through low supersonic flight regime in Fig. 3.14, as well as for the hypersonic flight regime in Fig. 3.15, were composed with results from wind tunnel tests, approximate design methods and numerical simulations [22, 23]. The lift coefficient C_L for subsonic Mach numbers shows linear behavior over a large range of angle of attack, Fig. 3.14 upper left. This can be compared against the HOPPER and HOPE-X, where nonlinear effects for $\alpha \approx 15$–$20°$ can be observed. The drag coefficient around $\alpha \approx 0°$ is very small for all Mach numbers, rising with increasing angle of attack as expected. The drag coefficient for transonic Mach numbers is largest, Fig. 3.14, upper right.

The maximum lift-to-drag ratio $L/D_{max} \approx 5$ occurs at $\alpha \approx 10°$ for subsonic Mach numbers and somewhat below 2° for in the low supersonic and hypersonic regimes, Figs. 3.14 and 3.15, both lower left. These values are somewhat lower than values found for HOPPER and HOPE-X.

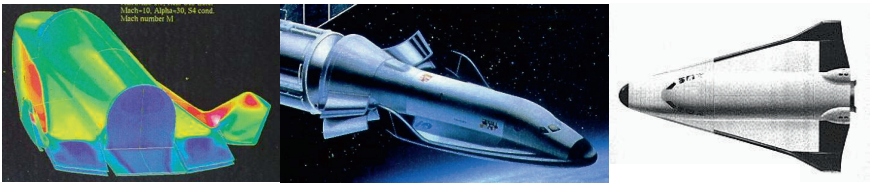

Fig. 3.13. HERMES shape 1.0: pressure distribution resulting from a numerical flow field simulation (left), synthetic image (middle), planform view (right) [22].

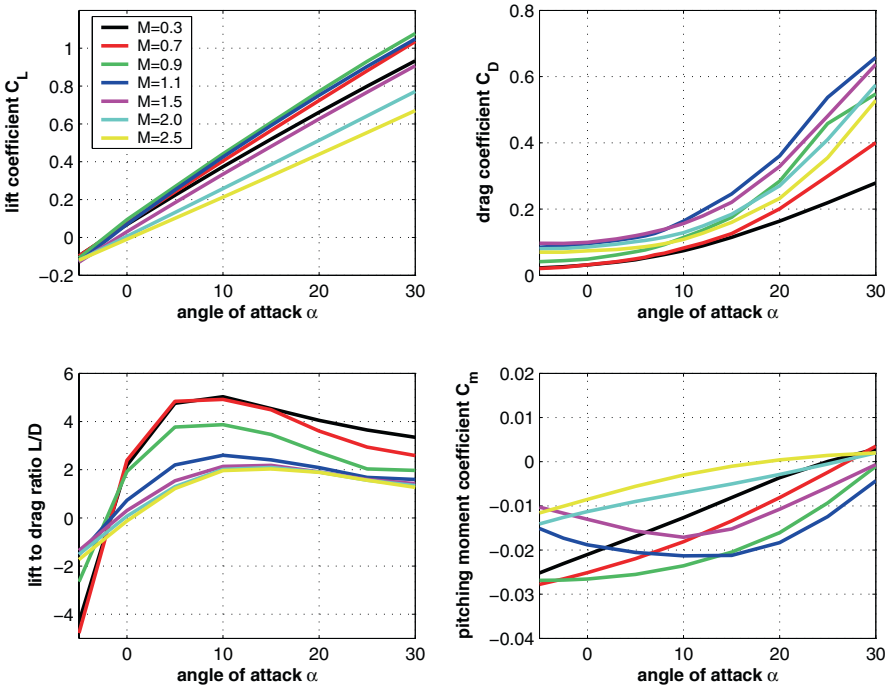

Fig. 3.14. Aerodynamic data of the HERMES shape 1.0 for the subsonic through low supersonic Mach number regimes, moment reference point $x_{ref} = 0.6\ L_{ref}$. Data source: [23].

The pitching moment data shown in Fig. 3.14 (lower right) indicate static stability for transonic/low supersonic Mach numbers ($1.1 \leqq M_\infty \leqq\leqq 1.5$) up to $\alpha \approx 10°$ but no trim point, and instability for subsonic and low supersonic Mach numbers. This behavior is essentially in agreement with the data of other vehicles discussed in this Section, see Figs. 3.18, 3.19, and 3.29. For higher supersonic and hypersonic Mach numbers, static stability and trim are observed for $\alpha \approx 40°$, Fig. 3.15, lower right. Mach number independence of C_L and C_D is seen for $M \gtrapprox 6$ to 8.

As an example of the effectiveness of the body flap, consider the example at $M_\infty = 10$, Fig. 3.16. With a positive (downward) body flap deflection one can shift the trim point to lower α values if the flight trajectory would require this. By applying a body flap deflection of $\eta_{bf} = 10°$, for example, the trim point is shifted from $\alpha \approx 38°$ to $\alpha \approx 27°$.

As will also be seen in Fig 3.31 for the HOPPER/PHOENIX shape, it is not unusual that a re-entry vehicle operates with negative body flap deflections in order to trim the vehicle, Sub-Section 3.4.2 and Sub-Section 6.1.2. This can be necessary since the free-stream conditions such as the Mach number, and

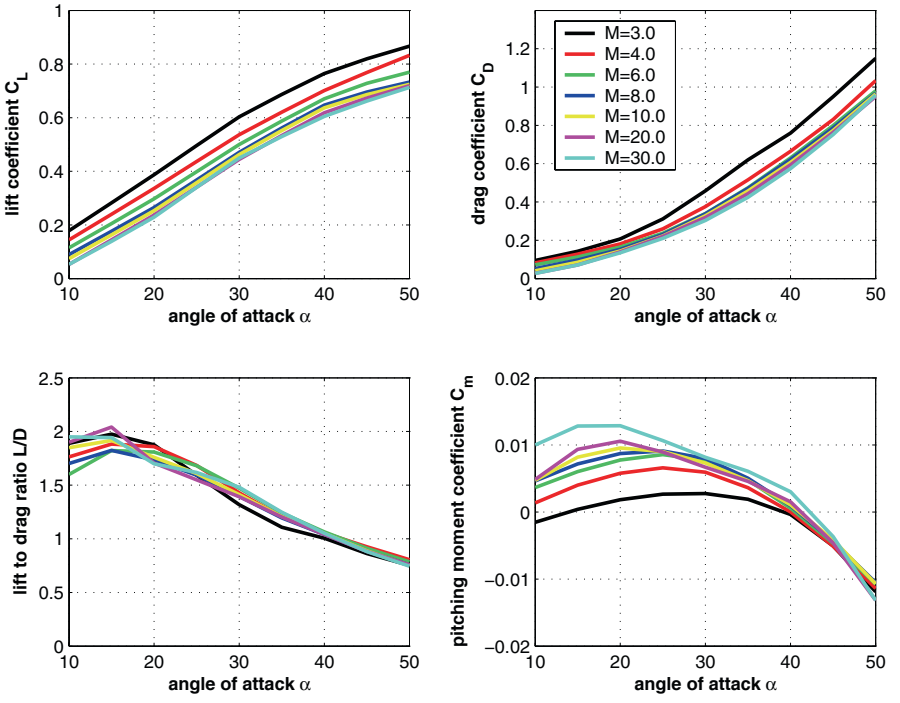

Fig. 3.15. Aerodynamic data of the HERMES shape 1.0 for the hypersonic Mach number regime, moment reference point $x_{ref} = 0.6\ L_{ref}$. Data source: [23].

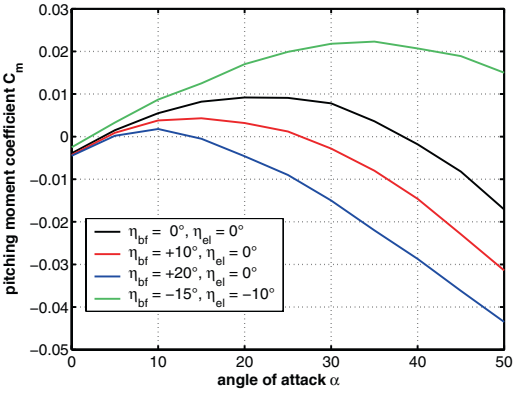

Fig. 3.16. HERMES shape 1.0, body flap and elevator efficiency for $M_\infty = 10$, moment reference point: $x_{ref} = 0.6\ L_{ref}$. Data source: [23].

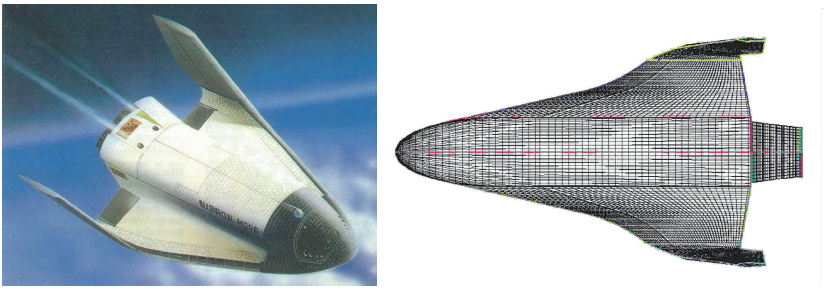

Fig. 3.17. HOPE-X shape: synthetic image, [24, 25]. Note that the shape of the synthetic image differs somewhat from that of the panel model.

the angle of attack, vary strongly over a wide range. In the HERMES project, investigations in this regard were carried out. Figure 3.16 shows that by deflecting the body flap by $\eta_{bf} = -15°$ and the elevators by $\eta_{el} = -10°$, the pitching moment increases strongly, which can help to trim the vehicle, especially at high angle of attack. The effect of flap-force reduction at negative flap deflection angle increases with increasing angle of attack, Sub-Section 6.1.2.

3.3.3 HOPE-X Configuration

In the 1980s, Japan joined the community of nations striving for an autonomous access to space. Besides rocket activities, Japan developed a conceptual re-entry vehicle called HOPE which was planned for payload transportation to and from the ISS. Due to budget constraints in the 1990s, this program was re-oriented to develop a smaller, lighter and cheaper vehicle, called HOPE-X, which was to operate unmanned, Fig. 3.17. The project was cancelled in 2003.

Figure 3.18 shows the aerodynamic data of longitudinal motion for subsonic and transonic Mach numbers. The lift coefficient of this vehicle with a slender wing is somewhat independent of the Mach number, indicating a behavior according to slender body theory [13].

The L/D values in the subsonic regime are similar to those of the HOPPER vehicle, Fig. 3.29, with a with a maximum of about 6 at $\alpha \approx 10°$. Also, the agreement of the pitching moment with its distinct static stability and trim behavior at $M_\infty = 1.1$ of the two shapes is noteworthy. Further, the marginally static stability for $0.8 \leqq M_\infty \leqq 0.9$ with the strong trend to become unstable at higher angles of attack should be emphasized. Beyond the transonic regime, say for $M_\infty \gtrapprox 1.1$, L/D_{max} drops for HOPE-X, like for all re-entry vehicles, to values not very much greater than 2, see also Figs. 3.14, 3.15, 3.18, 3.19, and 3.29.

The aerodynamic data for the supersonic and hypersonic Mach number regime, shown in Fig. 3.19, are the outcome of a set of approximate design methods, [24]. Mach number independence is present above $M_\infty \approx 6$. Again, a

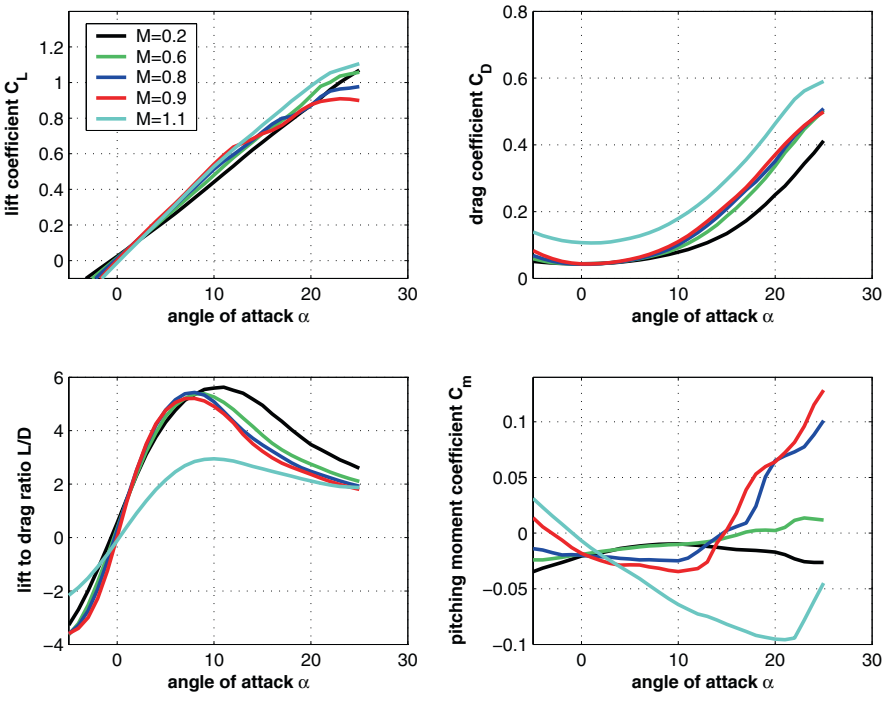

Fig. 3.18. Aerodynamic data of the HOPE-X shape for the subsonic and transonic Mach number regime. Data source: [24].

comparison with the data of the HOPPER configuration, Fig. 3.30, indicates the same trends.

Further we concern ourselves with the trim feasibility and the static stability of the vehicle. With a body flap deflection of $\eta_{bf} = 0°$, trim and static stability can be achieved for $M_\infty \geqq 4.0$ and $\alpha \geqq 30°$, Fig. 3.19. Application of a large body flap deflection of $\eta_{bf} = 30°$ leads to a corresponding nose-down pitching moment and a slight increase of the static stability, but creates a problem to trim the vehicle, Fig. 3.20, below. The same is still true when the center-of-gravity is shifted forward by 2.5 per cent, Fig. 3.20, above.

3.3.4 X-34 Configuration

In July 1996, NASA started a program with the goal of developing key technologies for transporting payloads and crews to space by using reusable launch vehicles. It was planned to prove these technologies in a realistic flight environment. For this reason, two demonstrators, the X-33 and the X-34 were developed. The X-34 concepts are shown in Fig. 3.21. For the X-33 no data are available, therefore, we discuss only available data of the X-34.

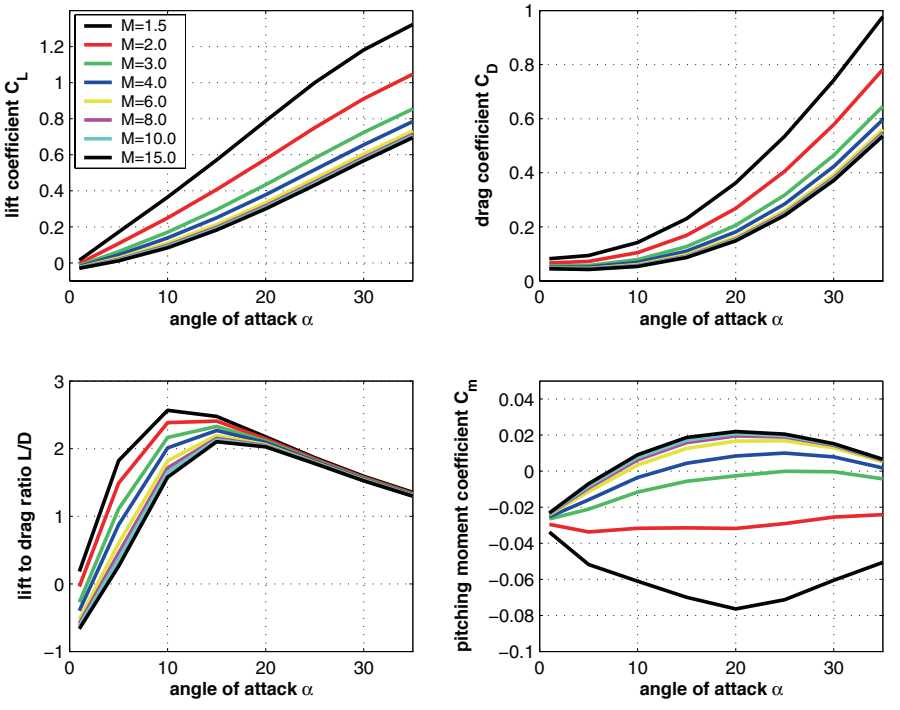

Fig. 3.19. Aerodynamic data of the HOPE-X vehicle for the supersonic and hypersonic Mach number regime. Data source: [24].

The mission profile of X-34 was as follows:

- captive carriage under the belly of a L-1011 aircraft up to an altitude of 11.5 km at a Mach number $M_\infty = 0.7$,
- drop-separation from a L-1011 aircraft,
- ignition of the rocket engine and acceleration to $M_\infty = 8$ at an altitude of 76.2 km,
- gliding back to Earth after engine burn-out, and execution of an autonomous landing on a conventional runway.

Some of the key technologies initially planned for demonstration were:

- lightweight composite airframe structures,
- advanced thermal protection systems,
- low cost avionics,
- automatic landing techniques.

In March 2001, NASA decided to terminate the technology program including test flying the X-34 vehicle.

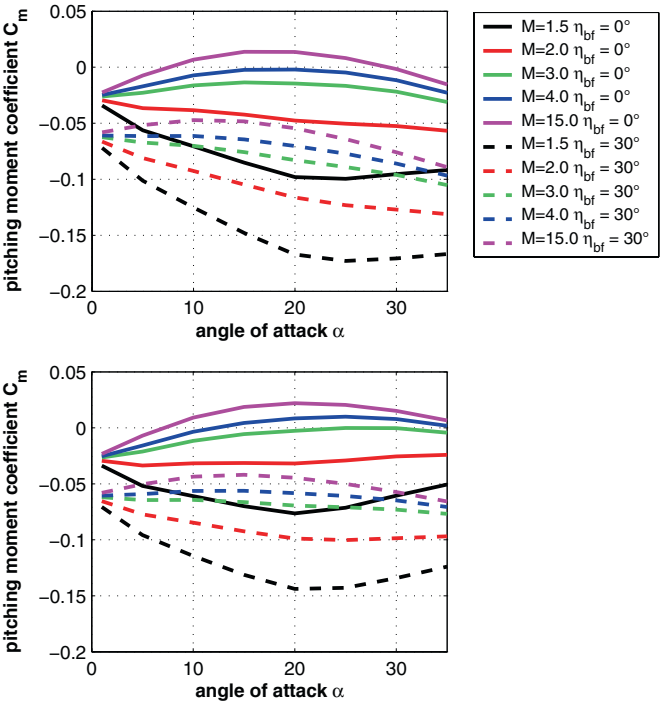

Fig. 3.20. Pitching moment behavior of the HOPE-X shape. Influence of the variation of the body flap angle η_{bf} for the nominal moment reference point (below), and for a moment reference point shifted 2.5 per cent forward (above). Data source: [24].

Fig. 3.21. X-34 shape: planform view (left) [26], synthetic image (middle), X-34 on NASA Dryden ramp (right) [27].

We present in Fig. 3.22 aerodynamic data of the X-34 vehicle which are essentially results from wind tunnel tests [26, 28, 29].

The first salient point is that the X-34 does not encounter stall for the angles of attack and Mach numbers considered, Fig. 3.22, upper left. This is similar to the behavior of HERMES, Fig. 3.14. Secondly, the slender X-34 vehicle achieves the highest maximum aerodynamic performance of all the vehicles considered in this section with $L/D \approx 7.2$ at $M_\infty = 0.3$.

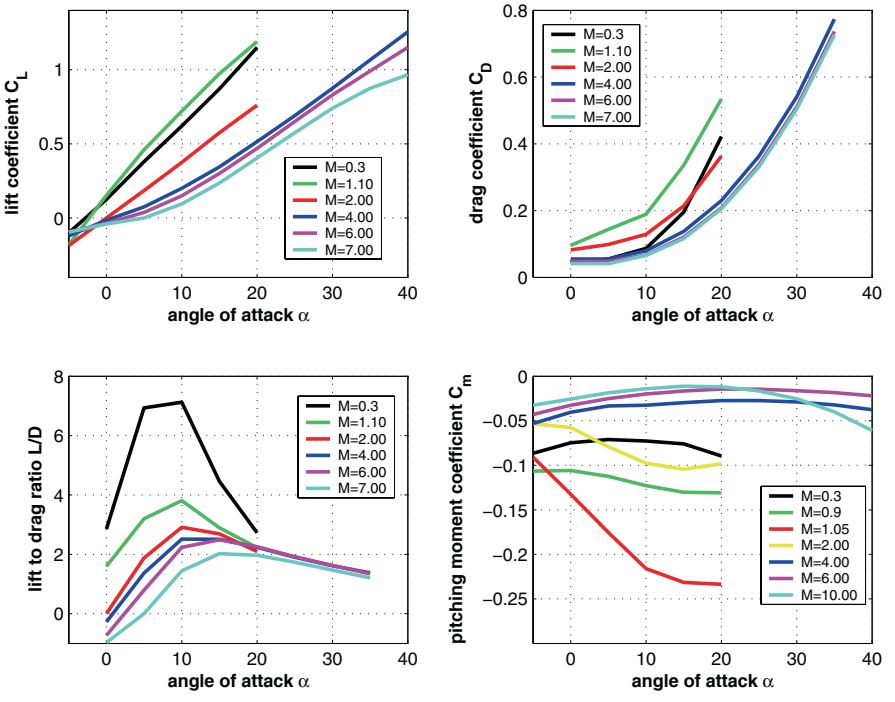

Fig. 3.22. Aerodynamic data of the X-34 shape for the subsonic to the hypersonic regime, moment reference point $x_{ref} = 0.6\ L_{ref}$. Data sources: [26], [28, 29].

The pitching moment follows the general trend of RV-W's with such shapes, i.e., that for the given center-of-gravity location, an instability is present at subsonic Mach numbers and small angles of attack, which turns to a strong static stability in the transonic and low supersonic regime. Further, for hypersonic Mach numbers we observe instability again which is due to increasing lift in the forward part of the vehicle, Fig. 3.22, lower right. In all cases, trim is not found due to the strong negative, zero-lift pitching moments. Mach number independence of the coefficients is seen for $M_\infty \gtrapprox 6$.

3.3.5 X-38 Configuration

In the 1990s, NASA envisaged the development of a Crew Return Vehicle (CRV) for the International Space Station. In case of illness of crew members or any other emergency, the CRV should be able to bring back to Earth up to seven astronauts. The essential point is that the crew return is done unpiloted, which means that the vehicle operates automatically. For this mission, a lifting body configuration, viz., the X-24A shape, was chosen and named X-38. The vehicle had to have the following features:

Fig. 3.23. X-38 shape, Rev. 8.3, planform view (left), vehicle #2 in free flight (middle), [27], model in wind tunnel (right) [30].

- accurate and soft landing to allow for the transportation of injured persons,
- load factor (n_t, n_n) minimization,
- sufficient cross range capability for reaching the selected landing site.

The X-38 is not a RV-W in the strict sense. As a lifting body, it glides like a winged re-entry vehicle, unpowered from an orbit along a given trajectory down to a specified altitude, but then conducts the final descent and landing by a steerable parafoil system. The parafoil system is a must because the aerodynamic performance L/D of such a lifting body in the subsonic flight regime is too low for an aero-assisted (winged) terminal approach and landing. The aerodynamic and aerothermodynamic characterization of the X-38 shape was made co-operatively by NASA, DLR (in the frame of the German technology programme TETRA)[12] and ESA, with Dassault Aviation as integrator of the activities [31].

To provide enough space for seven crew members, the X-24A shape was scaled up by a factor of 1.2 and the fuselage was redesigned on the leeward side to increase volume volume. The resulting shape, named X-38 Rev. 8.3, served as a technology demonstrator for the prototype CRV, see Fig. 3.23. In 2002 NASA changed its strategy and desired to pursue a multi-purpose vehicle, which could include both crew transport and crew return capabilities, instead of the single-purpose vehicle X-38. In June 2002, the X-38 project was cancelled.

All of the RV-W's considered so far in this section have the common feature that they are able to conduct an aero-assisted landing. This requires a minimum $L/D|_{max}$ value of between 4.5 and 5 in the low subsonic range. However, as mentioned above, the X-38 as a lifting body does not strictly belong to the class of RV-W's. Its value of $L/D|_{max} \approx 2$ in the subsonic regime and ≈ 1.3 in the higher supersonic regime, Fig. 3.24, lower left.

Further, the large pitching moment coefficients at small angles of attack are due to the strong boattailing of the lower side of the flight vehicle which can be seen in the lower right of Fig. 3.23.

Another obvious feature of the X-38's aerodynamics is its larger drag compared to HOPPER/PHOENIX and HERMES, Fig. 3.24, upper right. The

[12] Technologies for Future Space Transportation Systems, 1998–2001.

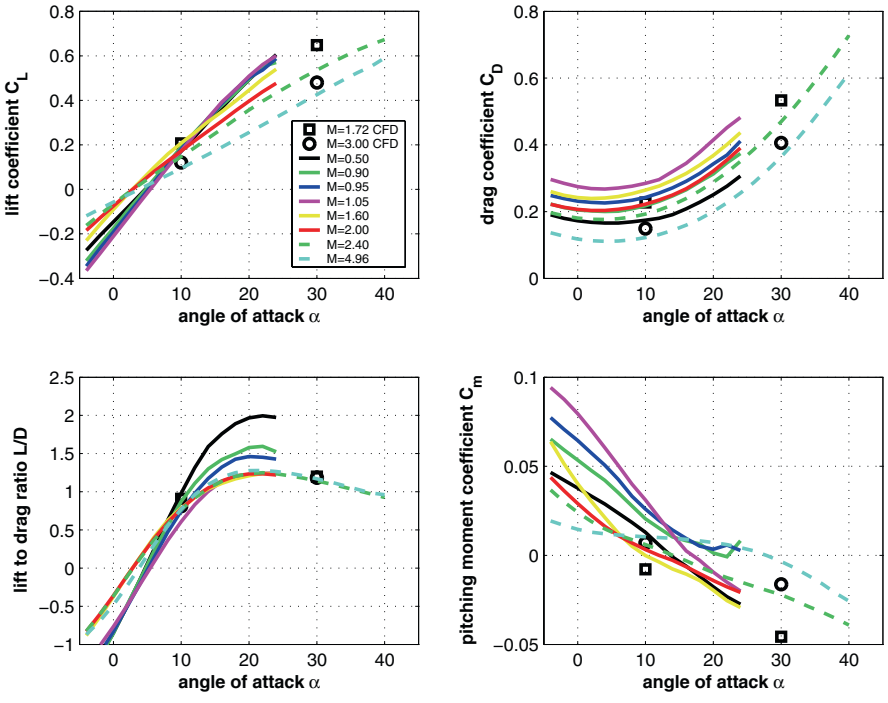

Fig. 3.24. Aerodynamic data of the X-38 shape, Rev. 8.3, for the subsonic, transonic and supersonic flight regime, moment reference point $x_{ref} = 0.57\ L_{ref}$, body flap deflection $\eta_{bf} = 20°$. Data sources: [32, 33].

data, taken from the Aerodynamic Data Book (ADB)[13] assembled by assembled by Dassault Aviation [32], were also verified by Euler computations for verification purposes [33] as seen in the figure. The agreement with the data from the ADB is rather good except for the pitching moment for $M_\infty = 1.72$, where some deviations occur.

A further comparison with laminar Navier–Stokes solutions at $M_\infty = 10, 15, 17.5$ at $\alpha = 40°$ is shown in Fig. 3.25. The following conclusions can be drawn:

- Wind tunnel data are remarkably well confirmed by the data from numerical flow simulation.
- The aerodynamic coefficients showed Mach number independence above $M_\infty \approx 6$.

A peculiarity is the behavior seen in the trim cross-plot, Fig. 3.26. Throughout the whole Mach number range, the vehicle behaves stably and can be trimmed,

[13] We present the data for a body flap deflection $\eta_{bf} = 20°$ since these more likely describe the nominal case than the data for $\eta_{bf} = 0°$.

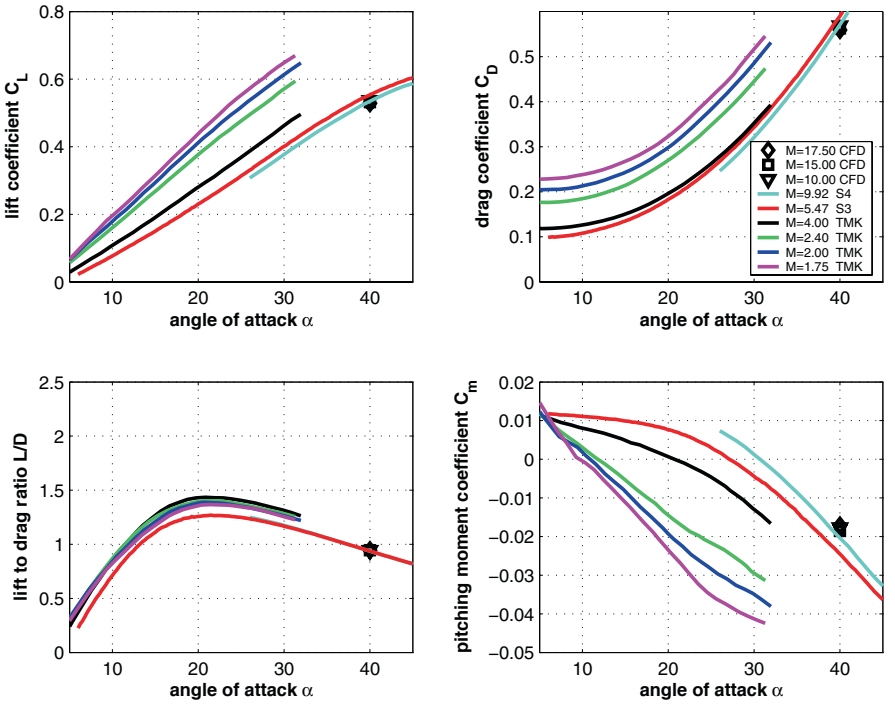

Fig. 3.25. Aerodynamic data of the X-38 Rev. 8.3 for the supersonic and hypersonic flight regimes, moment reference point $x_{ref} = 0.57\ L_{ref}$, body flap deflection $\eta_{bf} = 20°$. Data sources: [32, 34]–[36] .

which is different from the pitching moment characteristics of the RV-W's discussed before.[14] Further, it is interesting to examine the effectiveness of the body flap. Since the body flap deflection $\eta_{bf} = 20°$ is the nominal case, we concentrate on the two other cases $\eta_{bf} = 0°$ and $\eta_{bf} = 40°$. In the first case, $\eta_{bf} = 0°$, the pitching moment coefficient increases strongly compared to the nominal case, so that for the two lower Mach numbers of 0.5 and 1.05, trim can be achieved only for $\alpha \gtrapprox 25°$ which is not a realistic value. For the higher supersonic Mach number ($M_\infty = 4.96$), no trim and a reduced static stability can be observed. In the second case, a body flap deflection of $\eta_{bf} = 40°$, reduces strongly the pitching moment. The static stability grows and the trim points are shifted to much lower angle of attack.

[14] Note that this is a consideration in a sense different from those with the previously discussed RV-W's. There, arbitrary pitching moment data were discussed, i.e., for a given η_{bf}. Here, we study the actual trim capabilities of the vehicle.

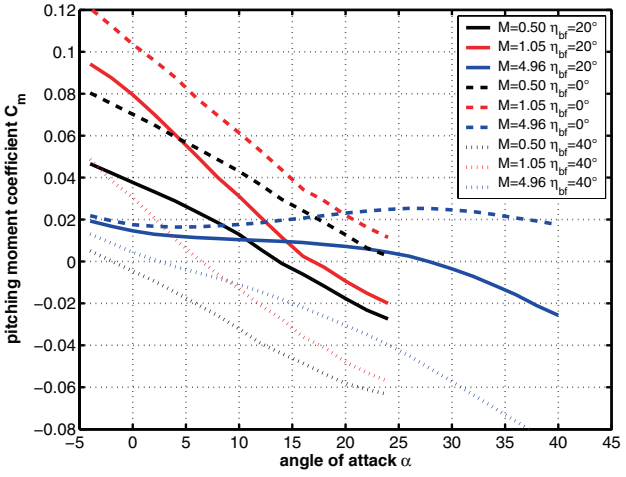

Fig. 3.26. X-38 shape, Rev. 8.3, pitching moment coefficient behavior for various body flap deflection angles η_{bf}, moment reference point $x_{ref} = 0.57\ L_{ref}$. Data source: [32].

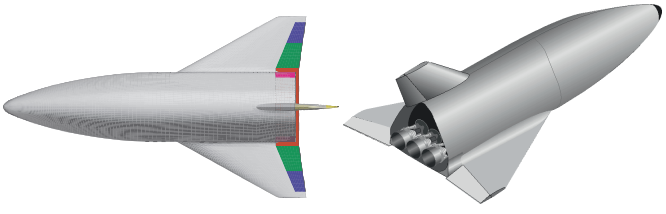

Fig. 3.27. HOPPER/PHOENIX shape. Synthetic images: planform view (left), 3-D view (right) [38, 39].

3.3.6 HOPPER/PHOENIX Configuration

In the frame of the "Future European Space Transportation Investigation Programme (FESTIP)," several Reusable Launch Vehicles (RLV) concepts were designed and developed with the goal of making access to space more reliable and cost effective. One of these concepts is the HOPPER vehicle, Fig. 3.27, which was foreseen to fly along a suborbital trajectory [37]. This means that this vehicle does not reach the velocity necessary for moving into an Earth target orbit. This also means that the vehicle is not able to return to its launch base, but has to fly to another landing ground. The main features of the system are the horizontal take-off (sled launch) and landing capability, and reusability. To demonstrate the low speed and landing properties of the vehicle shape,

Fig. 3.28. PHOENIX demonstrator: Test of subsonic free flight (helicopter drop test) and landing capability in Vidsel, Sweden in May 2004.

a 1 : 6 down-scaled flight demonstrator, called PHOENIX, was manufactured. PHOENIX was successfully flown[15] in 2004 in Vidsel, Sweden, Fig. 3.28.

The aerodynamic data set was established via tests in several wind tunnels and Navier–Stokes. Figure 3.29 shows the lift, drag and pitching moment coefficients as well as the lift-to-drag ratio for subsonic, transonic and supersonic flight Mach numbers. These data stem exclusively from wind tunnel tests.

As expected, $L/D|_{max} \approx 6$ occurs in the subsonic regime, dropping to $L/D|_{max} \approx 2$ in the supersonic regime. The pitching moment plot reveals static stability for the selected center-of-gravity position for all Mach numbers except $M_\infty = 3.96$. But trim for small positive angles of attack is only achieved for $M_\infty = 0.95$ and 1.1. The moment reference point with $x_{ref} = 0.68\, L_{ref}$ was found to be a realistic center-of-gravity position through a consideration of the internal layout of the vehicle.

The aerodynamic data for supersonic and in particular hypersonic Mach numbers, which were derived from Navier–Stokes solutions, are displayed in Fig. 3.30. For $M \gtrapprox 10$, lift and drag coefficients are nearly Mach number independent, but not the aerodynamic performance L/D. Further, as expected, the vehicle behaves statically unstable in the high Mach number regime for the neutral aerodynamic controls setting.

We describe now by which measures a vehicle can be trimmed to achieve longitudinal static stability if, for example, the pitching moment coefficient behaves like that of the HOPPER shape at $M_\infty = 3.96$, Fig. 3.29. Generally a positive (downwards) deflected body flap ($\eta_{bf} > 0$) causes an additional nose-down moment. However, a negative deflection ($\eta_{bf} < 0$) produces an additional nose-up moment, as can be seen in Fig. 3.31, right.

[15] Another European experimental vehicle, the Italian (CIRA) PRORA-USV, [40, 41], made its first balloon-launched transonic/subsonic flight in February 2007.

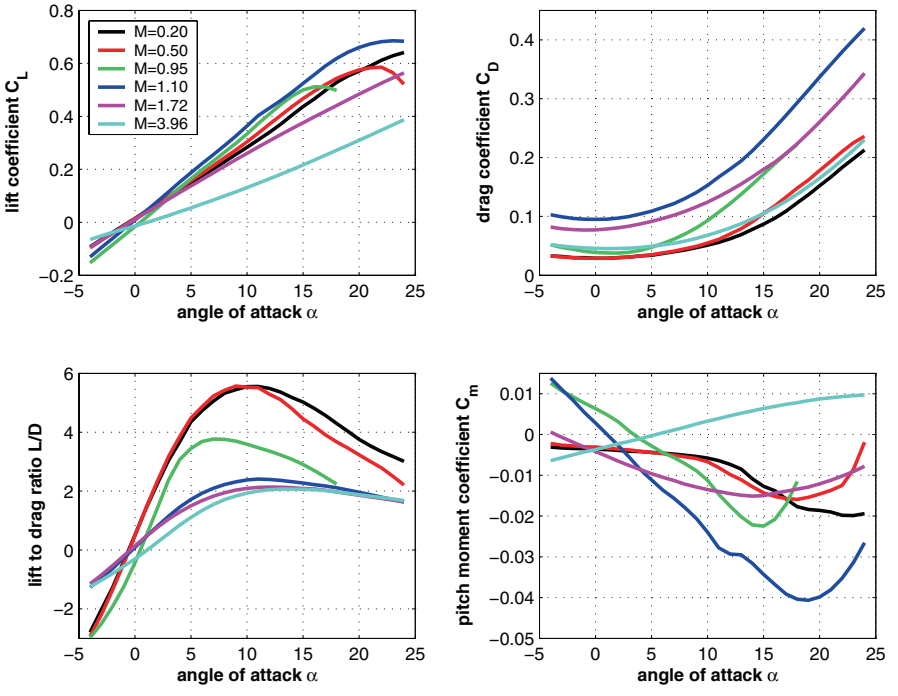

Fig. 3.29. Aerodynamic data of the HOPPER/PHOENIX vehicle for subsonic, transonic and supersonic Mach numbers based on wind tunnel measurements. Moment reference point $x_{ref} = 0.68\ L_{ref}$. Data source: [38].

Usually for re-entry vehicles flying along classical entry trajectories the angle of attack is $20° \lessapprox \alpha \lessapprox 30°$ for $M_\infty \approx 4$, Fig. 3.1. It seems that only for $\alpha \gtrapprox 30°$ a body flap deflection of $\eta_{bf} = +10°$ leads to a trimmed and stable flight situation. The other possibility for possibility for attaining static stability consists in a forward shift of the center-of-gravity, Fig. 3.31 (left). But in the case we consider here, the additional nose-down moment prevents trim for $\eta_{bf} = +10°$. Nonetheless, the vehicle behaves statically stable for $\alpha \gtrapprox 20°$ and can be trimmed with a body flap deflection $\eta_{bf} = -10°$ at $\alpha \approx 28°$.

3.3.7 Summary

We summarize now what the aerodynamic data of the considered RV-W's have in common and what differences exist.

- The lift coefficient in the transonic range ($0.8 \lessapprox M_\infty \lessapprox 1.2$) is, to different degrees, nonlinear for the Space Shuttle Orbiter, HOPE-X, X-38, and HOPPER/PHOENIX, Figs. 3.12, 3.18, 3.24, 3.29. Surprisingly, this is not

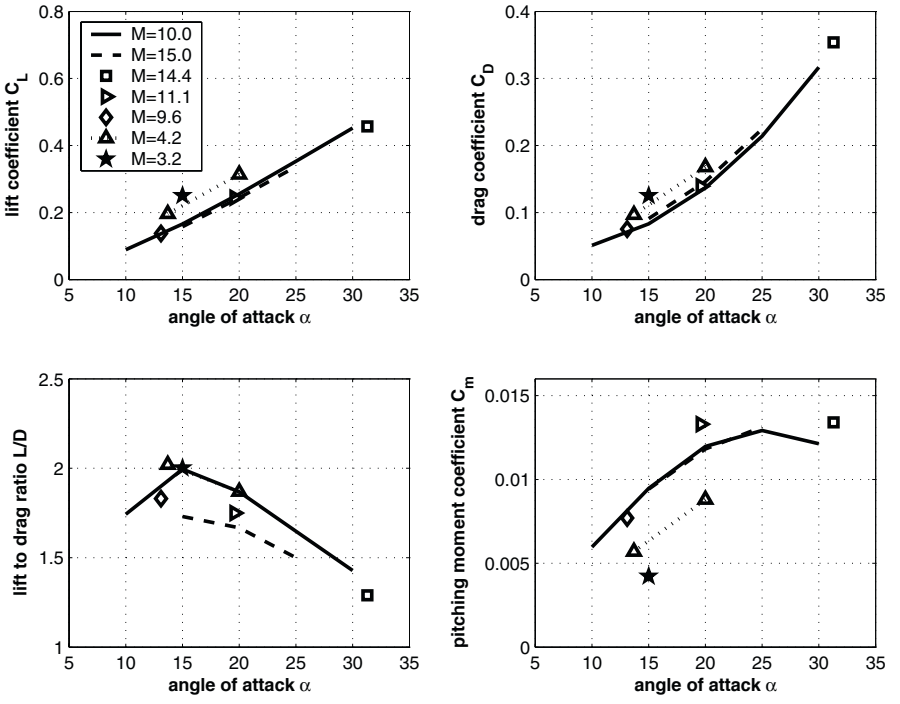

Fig. 3.30. Aerodynamic data of the HOPPER/PHOENIX vehicle for the supersonic and hypersonic Mach number regime based on CFD data. Moment reference point $x_{ref} = 0.68\ L_{ref}$. Data sources: [38, 39], [42].

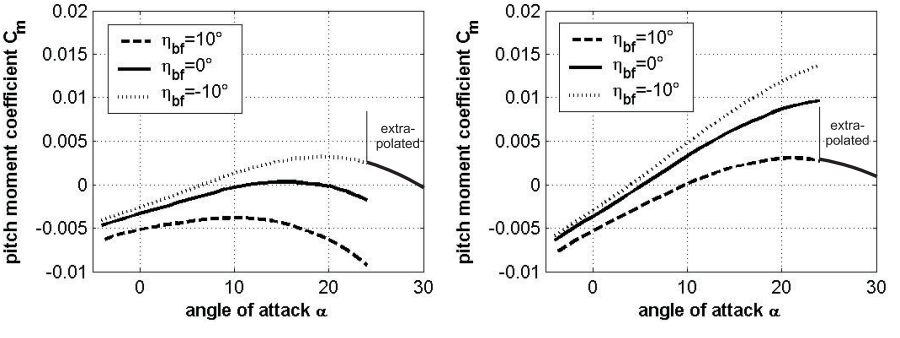

Fig. 3.31. Pitching moment behavior of the HOPPER/PHOENIX shape. Variation of the body flap angle η_{bf} for the nominal moment reference point $x_{ref} = 0.680\ L_{ref}$ (right), and for the moment reference point $x_{ref} = 0.655\ L_{ref}$ (left), $M_\infty = 3.96$. Data source: [38].

the case for HERMES, Fig. 3.14, and X-34, Fig. 3.22. This means that possibly lee side vortices either are not produced or do not play any role (vortex breakdown phenomena) for the pressure field on the upper body/wing surface.

- The drag and the lift coefficients are not monotonic with respect to the Mach number, but have a clearly marked maximum at $M_\infty \approx 1$. Figure 3.32 shows as example the behavior of the drag coefficients of all configurations at $\alpha = 20°$ as function of M_∞. They rise in the compressible subsonic domain, reach the transonic maxima, and then decrease with increasing M_∞, finally attaining Mach number independence at different Mach numbers that is dependent on the shape.
- The aerodynamic performance L/D is highest for low subsonic Mach numbers and reaches values well beyond 4 for the Space Shuttle Orbiter, HERMES, HOPE-X, X-34, and HOPPER/PHOENIX, Figs. 3.12, 3.14, 3.18, 3.22, 3.29. In the hypersonic regime, the maximum values diminish to $L/D \approx 2$. These observations do not apply to the X-38, since this is a lifting body which reaches a maximum $L/D \approx 2$ at medium subsonic Mach numbers, dropping to a value of $L/D \approx 1.3$ for hypersonic Mach numbers.
- The magnitude of the derivative of the pitching moment with respect to the angle of attack $dC_m/d\alpha$ has low positive to moderate negative values in the subsonic regime, grows to maximum negative values in the transonic regime and drops back to low negative or even positive values in the supersonic and hypersonic regime for $\alpha \lessapprox 20°$. This is more or less true for all shapes.
- The pitching moment depends on the position of the center-of-gravity and the deflection of elevators and body flaps.[16] But we can observe a clear tendency towards static stability in the transonic regime, Figs. 3.12, 3.14, 3.18, 3.22, 3.24, 3.29. In the hypersonic regime, the Space Shuttle Orbiter, HERMES, HOPE-X, X-34, and HOPPER/PHOENIX are statically unstable at lower angles of attack ($\alpha \lessapprox 20°$), but are statically stable at higher higher angles of attack, Figs. 3.12, 3.15, 3.19, 3.22, 3.30. This is in contrast to the X-38, which is statically stable throughout, Figs. 3.24 and 3.25.
- It is remarkable that the drag coefficients of HERMES, HOPE-X, and HOPPER/PHOENIX attain values at high supersonic and hypersonic Mach numbers which are very close together. The drag coefficients along the Mach number span of the Space Shuttle Orbiter and the X-34 are very similar which is not so surprising as a look at the planform of both vehicles indicates, Figs. 3.11 and 3.21.

[16] Also of speed brakes, if available in appropriate configuration.

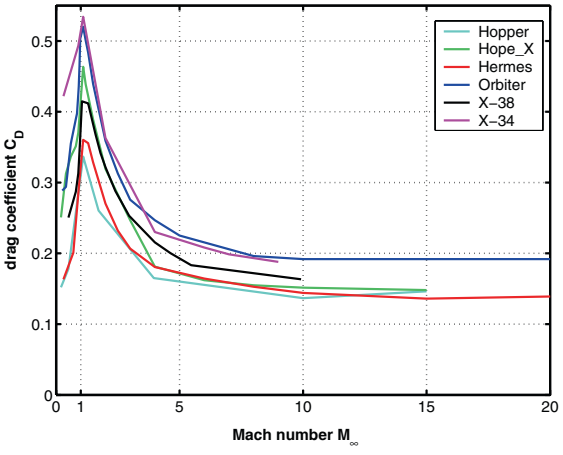

Fig. 3.32. Drag coefficient as function of the Mach number M_∞ at $\alpha = 20°$ for the vehicle shapes discussed in this section.

3.4 Vehicle Flyability and Controllability

3.4.1 General Considerations

Under flyability, we understand the fact that an air vehicle must be able to fly in a determinate way. Flyability means on the one hand that the vehicle can be trimmed. On the other hand, it concerns especially the stability about the lateral axis, which is called longitudinal stability, the directional stability about the vertical axis, and sufficient damping of roll motion around the longitudinal axis. Longitudinal and directional stability can be considered as weathercock stabilities, made possible in general by the provision of horizontal and vertical tail surfaces (stabilizers) respectively.

Regarding lateral stability of RV-W's we mention that a vertical stabilizer, like that on the Space Shuttle Orbiter, during the high angle of attack re-entry flight phase, Fig. 3.1, is in the "shadow" of the fuselage. Hence its effectiveness is severely curtailed. A possibility to avoid this effect is to provide winglets, Fig. 3.3, as was foreseen for HERMES [43]. With the Orbiter, the problem was alleviated by the use of the reaction control system, which is in any case needed for maneuvering in orbit. For further discussion of this and the above topics, see Section 2.1 and Chapter 6.

The movements about the axes of a moving aircraft are coupled to a certain degree, depending on the inertial properties of the airframe. Further, one also has to distinguish between static and dynamic stability. We will not go into these detailed discussions here but refer the reader to [44].

Under controllability, we understand that intended movements around all axes must be possible. This implies control surfaces of sufficient effectiveness

and sufficient "volume," the latter being the product of the area of the surface times the distance (lever arm) to the respective axis of the flight vehicle,[17] all in view of the requirements which are imposed by the respective moments of inertia of the vehicle. Detailed topics related to controllability, such as control surface aerothermodynamics, are treated in Chapter 6.

3.4.2 Trim and Stability of RV-W's

A RV-W is longitudinally trimmed by a deflection of one or more trim surfaces. These can be elevons and/or a body flap, Sub-Section 6.6.1. Downward deflection (η positive) causes an upward flap force and a nose-down (negative) increment of the pitching moment.[18] Upward deflection accordingly gives a downward flap force and a nose-up increment.

We now study aspects of these two trim modes in detail, with the vehicles flying at high angles of attack, and geometrically approximated as RHPM flyers, Figs. 3.33 (case 1, $\eta > 0$) and 3.35 (case 2, $\eta < 0$). In this approximation, the z-offsets (distances to the vehicle's x axis, Chapter 7) of both the center-of-gravity and the center-of-pressure, Section 7.1, are zero in the untrimmed case, and small and negligible in the trimmed case. We note that the force $\underline{F}_{aero,trim}$ in the figures is equal to the sum of all forces acting on the vehicle on the flight path, Fig. 2.5, found with a point-mass consideration. Here we consider the moment balance and nothing else.

Although actually elevons and/or a body flap may be employed, we use simply the term 'body flap' when speaking of the aerodynamic trim surface. The figures are schematics, and the flight path angles γ and the deflection angles of the body flap η_{bf} are exaggerated. Exaggerated too are the sizes of the body flap forces $\underline{F}_{bf}$, and the magnitudes of the trimmed forces $\underline{F}_{aero,trim}$ and the lift L and drag D components are not the same in both cases.

It is important to remember that in the untrimmed situation, the body flap is fixed in the neutral position $\eta_{bf} = 0°$, Section 3.3. This means that it contributes with $\underline{F}_{bf,\eta=0}$ to the force $\underline{F}_{aero}$. Hence $\underline{F}_{bf,\eta=0}$ must be vectorially subtracted from the flap force $\underline{F}_{bf}$, when the body flap is deflected, but also from $\underline{F}_{aero}$. We call the resulting flap force $\underline{F}_{bf,net}$.

In Figs. 3.33 and 3.35 we illustrate the subtraction schematically. We do not include the correct corresponding force polygons. The force $\underline{F}_{aero}$ is considered as reduced by $\underline{F}_{bf,\eta=0}$. The forces $\underline{F}_{bf}$ are assumed to act in the middle of the trim surfaces in direction normal to them.

In Fig. 3.33, we show schematically how longitudinal trim is achieved with the downward deflection of the body flap, $\eta_{bf} > 0$. The action line a_1 of the untrimmed lift force $\underline{F}_{aero}$ lies somewhat forward of the center-of-gravity where the trimmed force $\underline{F}_{aero,trim}$ acts. The action line a_2 of the net force of the body flap,

[17] The axes have their origin at the center-of-gravity of the vehicle.

[18] For the definition of aerodynamic forces and moments see Fig. 7.3, Section 7.1.

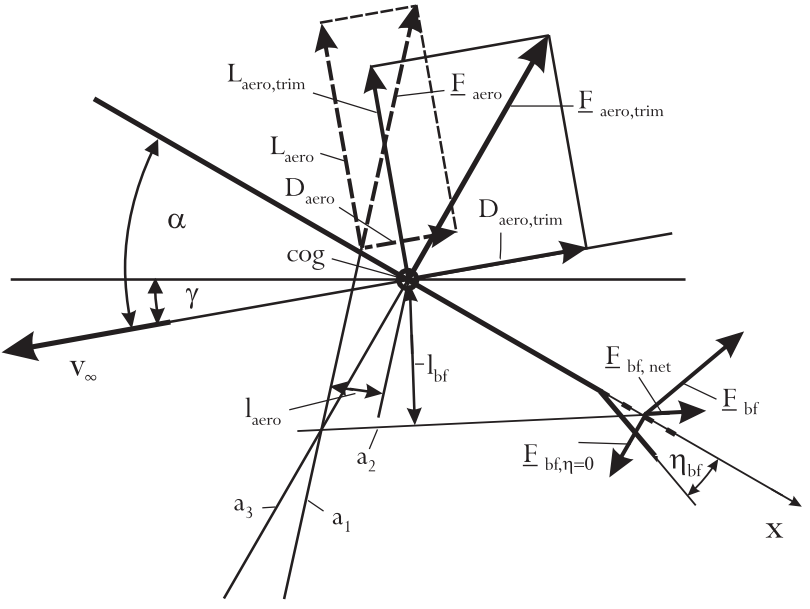

Fig. 3.33. Schematic of longitudinal trim of a RV-W at large angle of attack (geometrical RHPM approximation) with downward deflected body flap: involved force vectors $\underline{F}$ and lever arms l as well as lift L and drag D in untrimmed ('aero', broken lines) and trimmed ('aero,trim', full lines) situation. The action lines of the forces $\underline{F}$ are denoted by a_1 to a_3.

$$\underline{F}_{bf,net} = \underline{F}_{bf} + \underline{F}_{bf,\eta=0},$$

crosses a_1 below the center-of-gravity. Important is the observation, that trim is achieved, for this specific constellation, only if the action line a_1 of $\underline{F}_{aero}$ lies forward of the center-of-gravity, which then results in the moment balance

$$l_{aero}|\underline{F}_{aero}| = l_{bf}|\underline{F}_{bf,net}|.$$

Figure 3.33 also illustrates how the downward deflected trim flap creates the aerodynamic trim force $\underline{F}_{bf,net}$. This force added to $\underline{F}_{aero}$ gives the trimmed aero force

$$\underline{F}_{aero,trim} = \underline{F}_{aero} + \underline{F}_{bf,net},$$

see Fig. 3.34a). The action line a_3 of $F_{aero,trim}$ crosses the center-of-gravity, which is now also the center-of-pressure. The resultant moment around the center-of-gravity is zero and the vehicle is trimmed.

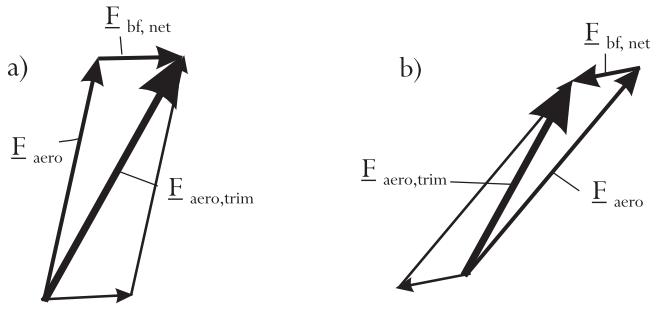

Fig. 3.34. Force polygons: cases a) with downward and b) with upward deflected body flap.

Because the original untrimmed force $\underline{F}_{aero}$ acts ahead of the center-of-gravity, the vehicle flies trimmed, but statically unstable.[19] The static margin is negative and approximately equal to l_{aero} in Fig. 3.33.[20]

However, a situation can also be found in RV-W's where the body flap/elevons are deflected upwards, Sub-Section 6.1.2. We show this situation without a detailed discussion in Figs. 3.35 and 3.34b). Now, the original untrimmed force $\underline{F}_{aero}$ acts downstream of the center-of-gravity. Therefore, with the upward deflected body flap, the vehicle flies trimmed and statically stable. The static margin is positive and approximately equal to l_{aero} in Fig. 3.35.

Although we have considered the RV-W at large angle of attack only in the geometrical RHPM approximation, the results can be generalized:

- Downward deflection of body flap/elevons means trimmed but statically unstable; upward deflection trimmed but statically stable flight of the vehicle.
- In the statically unstable case $L/D|_{aero,trim} < L/D|_{aero}$, Fig. 3.33 (compare also Figs. 3.12 and 2.3). This holds also for the statically stable case, Fig. 3.35.
- If the vehicle is statically unstable, lift L and drag D are larger in the trimmed than in the untrimmed case, Figs. 3.33 and 3.34a), but smaller, if the vehicle is statically stable, Figs. 3.35 and 3.34b).

[19] This is in contrast to classical aircraft which fly stably. There the longitudinal trim is achieved by horizontal surfaces (elevators), which have a negative angle of attack and exert a downward force.

[20] In the literature one finds sometimes that this case, i.e., the untrimmed force $\underline{F}_{aero}$ acting ahead of the center-of-gravity, is considered to have a positive static margin.

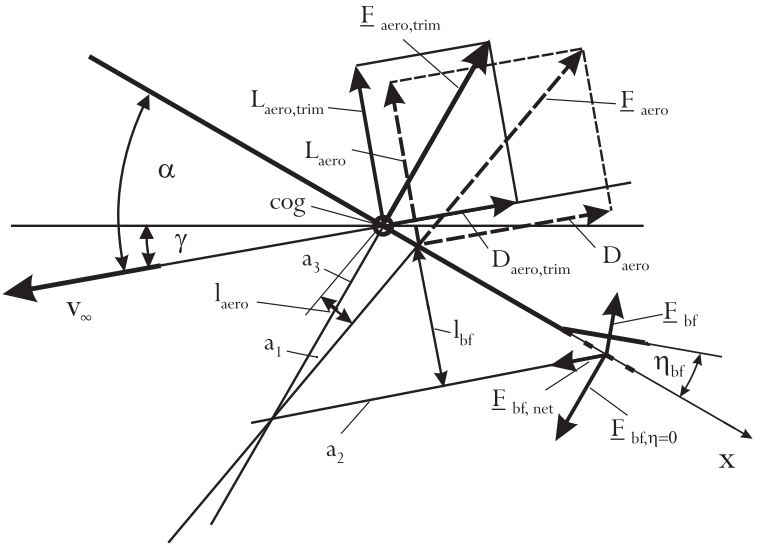

Fig. 3.35. Schematic of longitudinal trim of a RV-W vehicle (geometrical RHPM approximation) at large angle of attack with upward deflected body flap. For details, see Fig. 3.33.

3.5 The Hypersonic Pitching Moment Anomaly of the Space Shuttle Orbiter

During the first flight of the Space Shuttle Orbiter (STS-1), the so-called hypersonic pitching moment anomaly was manifested up. This is due to the pitch-up moment being larger than predicted in the high flight Mach number domain. This situation required a (downward) body flap[21] deflection, which was more than twice as large as predicted, Fig. 3.36 [45]. Together with the pitching moment discrepancy, a discrepancy between the predicted and the actual normal force was also observed. Angles of attack corresponding to the flight Mach numbers in Fig. 3.36 are, with small departures, $\alpha = 40°$ from $M_\infty \approx 24$ down to $M_\infty \approx 10$, and $\alpha = 25°$ at $M_\infty \approx 5$, see [46] and also Fig. 3.1 of this book.

Figure 3.36 shows that the largest deviation (factor approximately two) from the predicted body flap deflection angle occurs from $M_\infty \approx 17$ to $M_\infty = 24$. Below $M_\infty \approx 8$, predicted and flight data are, with some noteworthy exceptions, close to each other.

It can be a useful exercise for the reader to deduce the free-stream data, at least approximately, from the altitude-velocity map, Fig. 2.2 and the atmospheric data given in Appendix B, and to compare them with the data from [47].

[21] Originally the body flap was to act as a heat shield for the nozzles of the main engines of the Orbiter, now it became the primary longitudinal trim device [48].

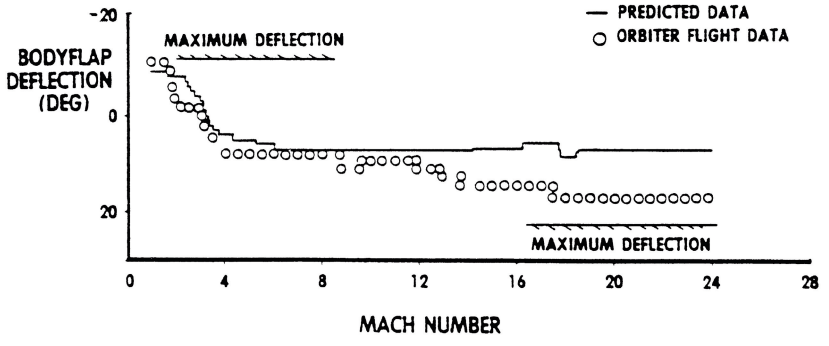

Fig. 3.36. Predicted and flight data of body flap deflection for trim as function of the flight Mach number of the first flight (STS-1) of the Space Shuttle Orbiter [45].

What caused this "anomaly," which was subsequently extensively studied [17, 18]? Before we discuss the problem in detail, we look at the trim situation and list possible causes of the anomaly.

3.5.1 Trim Situation and Possible Causes of the Pitching Moment Anomaly

Investigations after the first mission of the Space Shuttle Orbiter revealed that the actual center-of-pressure location was further forward than derived from ground simulation and numerical modeling before flight.[22] This means that the action line a_1 in Fig. 3.33 of the untrimmed lift force $\underline{F}_{aero}$ would lie even further forward than shown in that figure. It is evident that this induces an additional nose-up moment. It is also evident that a larger downward deflection angle of the trim flap was necessary to trim the vehicle, Fig. 3.36.

We now consider the aerodynamic surface forces acting on the vehicle and causing forces and moments, regarding only the longitudinal motion. These surface forces are basically the wall pressure p_w and the skin-friction τ_w, Fig. 3.37. It is important to note that the wall pressure can be increased by hypersonic viscous interaction [1]. Hypersonic viscous interaction can occur during hypersonic flight at high altitudes, where large local Mach numbers in combination with low unit Reynolds numbers (both defined at the boundary layer edge) lead to thick boundary layers which then induce an additional wall pressure.

Neglecting p_w and τ_w in the "shadow" parts of the configuration (indicated by broken lines), the forces on the vehicle and the contributions of p_w and τ_w to them are basically, though very approximately:

– the lift which is the force in direction normal to the flight path $L = L(p_w, \tau_w)$,

[22] At $\alpha = 40°$, this was approximately 0.3 m in the numerical simulation of [14], which amounts to a little bit less than 1 per cent body length.

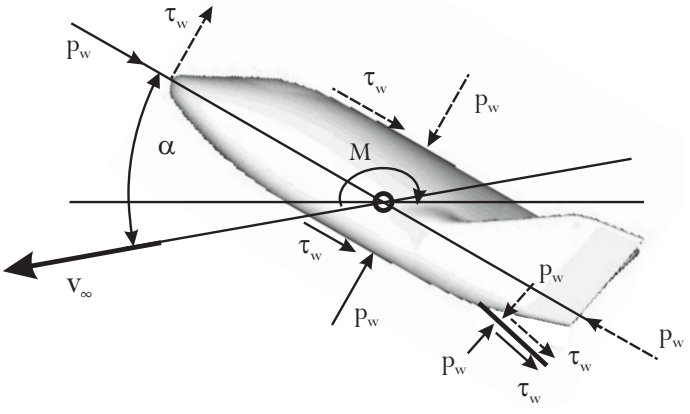

Fig. 3.37. Longitudinal motion: schematic of the wall pressure p_w and the skin-friction τ_w acting on the surface of a RV-W (broken lines: small forces which can be neglected in the considerations). Not indicated are the integral forces: lift, drag, etc.

- the drag which is force in direction of the flight path $D = D(p_w, \tau_w)$,
- the axial force which the force in direction of the vehicle axis $A = A(p_w, \tau_w)$,
- the normal force which is the force in direction normal to the vehicle axis $N = N(p_w, \tau_w)$,
- the trim force on elevons/body flap $F_{trim} = F_{trim}(p_w, \tau_w)$,
- the pitching moment moment $M = M(p_w, \tau_w)$, which is zero if the vehicle is trimmed.

It is noteworthy that the aerodynamic performance of the Orbiter in the hypersonic flight domain was well predicted as demonstrated in the first flight except for the normal force N and the longitudinal trim characteristics [45].

Major possible effects that were not adequately taken into account in the aerodynamic data base were seen and studied:[23]

- High temperature real gas and Mach number effects[24] [14, 49]–[53].
- Viscous forces and effects, including hypersonic viscous interaction, regarding both airframe and trim surface aerodynamics [14, 54, 55]. Trim surface and elevon effectiveness can also be adversely affected by erroneous bow shock shapes in ground facility simulations [14].[25]

Other factors potentially having played a role are [14]:

- Insufficient knowledge of actual atmospheric properties, especially air density, during re-entry.

[23] Only a few papers are cited.

[24] This is connected to the extent that Oswatitsch's Mach number independence principle for blunt bodies is valid in ground facility simulations.

[25] Trim surface effectiveness, however, obviously was sufficient, see the discussion on page 309 of this book.

– Uncertainties in the actual location of the center-of-gravity of the flight vehicle.
– Possible small aerodynamic shape difference between the actual flight vehicle and the ground-facility simulation models.

3.5.2 Pressure Coefficient Distribution at the Windward Side of the Orbiter

Remember, that except for the pitching moment and the normal force, all aerodynamic forces and moments were predicted sufficiently well. We assume therefore that it is sufficient to study only the wall pressure distribution at the lower side (windward side) of the Orbiter in view of the pitching moment anomaly, taking into account the configurational particularities of the lower side of the vehicle. The wall pressure is the most important force acting on the windward side of the vehicle. Unfortunately, no detailed information about the other forces is available.

Early viscous computations on simple shapes had shown that high temperature real gas effects reduce aerodynamic forces and the (nose-up) pitching moment [49].[26] On the other hand, viscous forces, i.e., the wall shear stress, acting mainly on the windward side of the flight vehicle, will induce a pitch-down increment, as can be deduced from Fig. 3.37.

We now investigate the pressure coefficient distributions along the lower symmetry line of the vehicle at two angles of attack. The computations for the two cases[27] taken from [49] ($\alpha = 25°$, inviscid, Fig. 3.38) and [51] ($\alpha = 40°$, viscous, Fig. 3.39) were made with a modified vehicle configuration.[28] We use $M_\infty = 10$ with perfect gas ($\gamma = 1.4$) as the reference pre-flight case and $M_\infty = 24$ with equilibrium/non-equilibrium gas model as the reference post-flight case.

During the aerodynamic shape definition process of the Orbiter, it was observed that high temperature real gas effects reduce c_{p_w} on the lower (windward) surface of the vehicle. This observation does not hold where a re-compression after an overexpansion takes place. In the $\alpha = 25°$, case this is at 300.0 in. $\lessapprox Z \lessapprox$ 450.0 in. on the centerline, Fig. 3.38. If we change our notation

[26] Regarding the high temperature real gas effects, numerical studies in the aftermath of the discovery of the hypersonic pitching moment anomaly show a different picture, which possibly is due to the particular shape of the lower side of the vehicle.

[27] We have noted above, that the flight Mach number at $\alpha = 25°$ is $M_\infty \approx 5$. In [49] results are presented—obviously due to the limited computation capabilities at that time—for this angle of attack, though for flight Mach numbers which belong to the $\alpha = 40°$ regime. However, for high flight Mach numbers $\alpha = 25°$ is included in the aerodynamic design data book of STS-1 [20]. We keep the $\alpha = 25°$ case in the following investigations in order to widen our data base.

[28] This was necessary because of the weak computer resources in 1983 and still in 1994. Later, investigations with the full geometry were made [53].

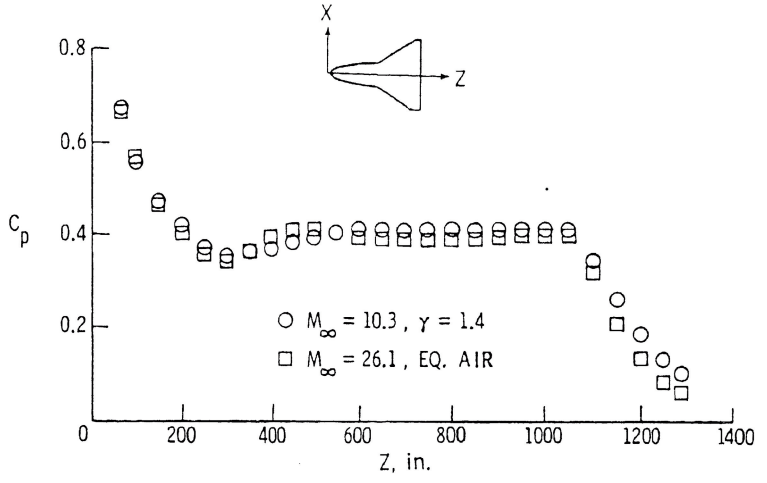

Fig. 3.38. Wall pressure coefficients c_{p_w} along the windward symmetry line of the Orbiter configuration [49]. Angle of attack $\alpha = 25°$, inviscid computations.

from Z to x, this amounts to $0.23 \lessapprox x/L \lessapprox 0.35$.[29] Note that at this location, the longitudinally flat surface part of the windward side of the vehicle begins. This location is also approximately where the crossover of c_{p_w} as function of M_∞ and high temperature real gas effects, mentioned in Sub-Section 3.2.1, occurs.

In the $\alpha = 40°$ case, the re-compression occurs slightly ahead of that region, Fig. 3.39. The reduction of c_{p_w}, however, is strongest in the region $1,060.0$ in. $\lessapprox Z \leqq 1,290.3$ in. $(0.82 \lessapprox x/L \leqq 1.0)$. The authors of [49] remark that other unpublished results indicate only weak Mach number effects, i.e., Mach number independence, so that the differences in c_{p_w} probably can be attributed mainly to high temperature real gas effects.

Before we analyze both cases together, we note two points regarding the $\alpha = 40°$ case, Fig. 3.39. Firstly, the figure was made with an axis convention different to that of Fig. 3.38. The stagnation point lies at $z = 0$ in. $(x/L = 0)$ at the right-hand side, whereas the end of the vehicle lies at $z = -1,290$ in. $(x/L = 1)$ at the left-hand side. Secondly, the non-dimensional pressure $p/\rho_\infty v_\infty^2 = p_w/(2q_\infty)$ in Fig. 3.39 can be converted into the pressure coefficient c_p by means of the relation:

$$c_p = c_{p_w} = \frac{p - p_\infty}{q_\infty} = \frac{2\,p}{\rho_\infty v_\infty^2} - \frac{2}{\gamma_\infty M_\infty^2}. \tag{3.9}$$

[29] $L = 32.7736$ m $= 1{,}290.3$ in. is the length of the Orbiter without the 2.21 m (87.0 in.) long body flap [48].

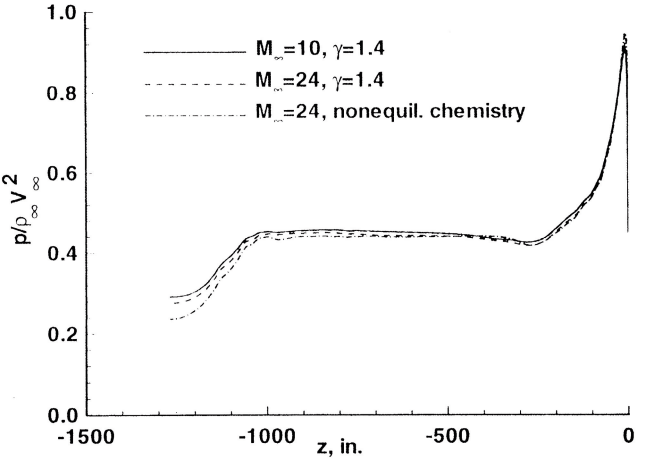

Fig. 3.39. Wall pressure $p/\rho_\infty v_\infty^2$ ($\equiv p_w/\rho_\infty v_\infty^2$) along the windward symmetry line of the Orbiter configuration [51]. Angle of attack $\alpha = 40°$, viscous computations for wind tunnel and for flight at $H = 70$ km altitude.

The overall pattern of the pressure distribution on the windward symmetry line in the $\alpha = 40°$ case (Fig. 3.39) is quite similar to that in the $\alpha = 25°$ case (Fig. 3.38).

The reader is now asked to note in both figures the pressure plateau[30] at $0.4 \lessapprox x/L \lessapprox 0.82$, and the strong drop of c_{p_w} at $0.82 \lessapprox x/L \leqq 1$. In order to understand these properties of the pressure field, consider Figs. 3.40 and 3.41. We see from the first of these figures that the lower surface of the flight vehicle is flat in longitudinal direction in the range $0.12 \lessapprox x/L \lessapprox 0.82$. Boattailing begins at $x/L \approx 0.82$ with an angle of approximately 6°. Boattailing of a fuselage usually is applied in order to increase the scrape angle for take-off and landing, to influence (in low speed flight) the vehicle's pitching moment, and to reduce the base area (hence the base drag). Further, Fig. 3.41 shows a slight positive (upward) dihedral of the lower side of the vehicle. Such a dihedral shape improves rolling and also lateral/directional stability [44]. Behind $x/L \approx 0.62$, the lower side, approximately below the fuselage, is rather flat.

Hence for $0.4 \lessapprox x/L \lessapprox 0.82$, the lower side of the flight vehicle can be considered as approximately flat, except for the dihedral area of the outer wing, Fig. 3.6. This means that, for the angle of attack regime considered in this section, the flow there—initially between the primary attachment lines—is approximately two-dimensional in nature, as is discussed in Sub-Section 3.2.2. This can also be seen from earlier computational and oil-flow data [51, 53, 55].

We come now back to the behavior of c_{p_w} in Figs. 3.38 and 3.39. The pressure plateaus at $0.4 \lessapprox x/L \lessapprox 0.82$ obviously are due to the longitudinal flatness

[30] We switch completely over from the Z notation to the x or, equivalently, the x/L notation.

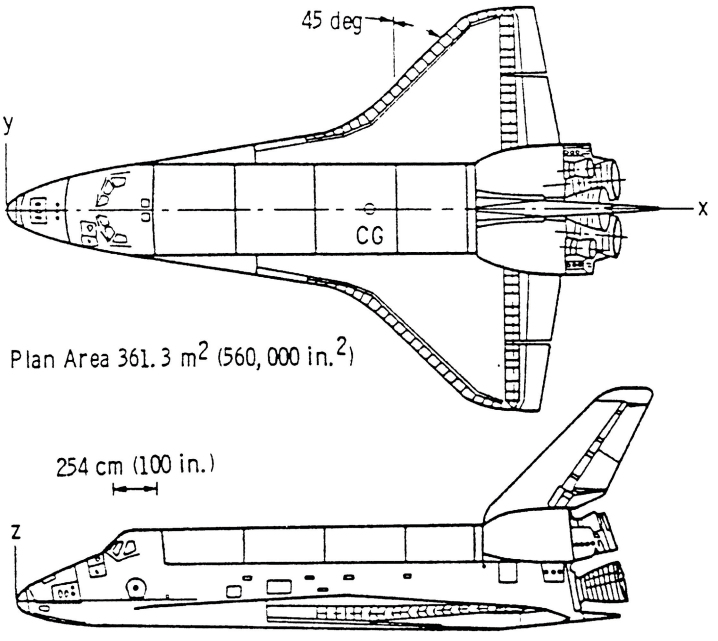

Fig. 3.40. Plan and side view of the Orbiter [14].

of the lower side of the flight vehicle. We assemble the c_{p_w} data (case 1.a and 1.b from Fig. 3.38 and case 2.a to 2.c from Fig. 3.39) at the location $x/L = 0.62$ in Table 3.4.

We see that in case 2.b, c_{p_w} is slightly larger than that in case 2.a. It is not quite clear what is to be expected. Note that the data from Fig. 3.39 had to be converted with the help of eq. (3.9). Usually in this part of the configuration, for a given angle of attack, the wall pressure coefficient c_{p_w} decreases with increasing M_∞ and with the presence of high temperature real gas effects. At the forward stagnation point (data are not shown in the table), we expect, according to Fig. 3.5 in Sub-Section 3.2.1, that c_{p_w} is largest for the highest Mach number and with high temperature real gas effects present. This is indicated for the $\alpha = 40°$ case in Fig. 3.39.

In [1], it is discussed that the windward side boundary layer on a RV-W at large angle of attack is initially a subsonic, then a transonic and finally a low supersonic boundary layer.[31] The boundary layer edge Mach numbers are rather small. In [56], it is reported that during an Orbiter re-entry, these are typically at most $M_e \approx 2.5$ and mostly below about 2. Hence, we assume that

[31] This boundary layer is characterized by very high temperatures and hence high temperature real gas effects, by strong wall-normal temperature gradients due to surface radiation cooling and is, depending on the TPS, influenced by surface roughness.

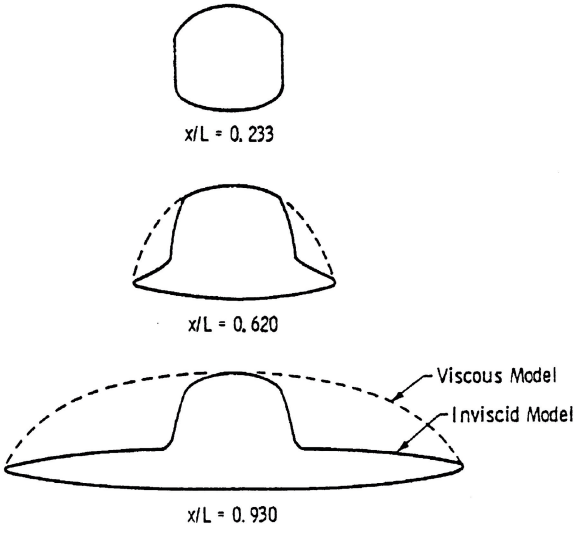

Fig. 3.41. Cross sections of the simplified Orbiter geometry (Viscous Model = HALIS configuration) [14].

Table 3.4. Wall pressure coefficients c_{p_w} in the lower symmetry line of the Orbiter at $x/L = 0.62$ for $\alpha = 25°$ (Fig. 3.38) and $\alpha = 40°$ (Fig. 3.39).

Case	Fig.	α	M_∞	γ	x/L	c_{p_w}
1.a	3.38 (invisc.)	25°	10.3	1.4	0.62	0.41
1.b	3.38 (invisc.)	25°	26.1	equil.	0.62	0.38
2.a	3.39 (visc.)	40°	10	1.4	0.62	0.89
2.b	3.39 (visc.)	40°	24	1.4	0.62	0.90
2.c	3.39 (visc.)	40°	24	non-eq.	0.62	0.88

we have supersonic flow in the $\alpha = 25°$ case, but low supersonic flow in the $\alpha = 40°$ case.

This is important, because the boattailing, which begins at $x/L \approx 0.82$, leads to a flow expansion only if the flow ahead of it is supersonic. Such a situation is present even at the large angles of attack during the initial re-entry flight phase. The effect can be understood and approximated basically with the help of the Prandtl–Meyer expansion [1], or understood qualitatively in terms of the stream-tube behavior [13]. However, behind $x/L \approx 0.82$ the pressure coefficient drops further, therefore we have neither a "centered" nor a "simple"

expansion [1]. One could speak of a "distributed simple" expansion due to the initially curved boattailing, Fig. 3.40.

In cases where the plateau wall Mach numbers are subsonic (angles of attack larger than considered here), one can assume that the pressure would increase in the boattailing region and induce a nose-down increment of the pitching moment. A "pitching moment reversal" is indeed present for $\alpha \gtrapprox 50°$ [57]. In the literature, see for instance [53], it usually is not attributed to a boattailing re-compression due to a subsonic plateau Mach number.

We consider now the situation in the boattailing region $0.82 \lessapprox x/L \leqq 1$. In Figs. 3.38 ($\alpha = 25°$) and 3.39 ($\alpha = 40°$), we see that there are quantitative differences in the c_{p_w} behavior compared to that in the upstream pressure plateau region. In the boattailing region, the differences in c_{p_w} become much larger when we go from the lower flight Mach number cases with perfect gas to the higher flight Mach number cases which take into account high temperature real gas effects. Remembering the remark in [49] that Mach number effects were found to be small (Mach number independence), these differences can then be attributed mostly to high temperature real gas effects.

Whether the assumption of equilibrium or non-equilibrium behavior of the gas plays a role cannot be decided with the available data. The $M_\infty = 24$ case corresponds to a flight altitude of about 72 km. Considering the length of the pressure plateau on the windward side of the flight vehicle $0.4 \lessapprox x/L \lessapprox 0.82$ which amounts to approximately 14 m, one can assume that thermo-chemical equilibrium is attained in the inviscid flow part of the shock layer. We come back to the influence of flight Mach number and high temperature real gas effects in Section 3.6, considering then also the influence of the two different angles of attack.

For the quantitative study of the situation in the boattailing region, data are collected in Table 3.5. There c_{p_w} data (cases 1.a and 1.b from Fig. 3.38 and cases 2.a to 2.c from Fig. 3.39) are given for the location $x/L = 0.91$ which is approximately the middle of the boattailing region. We see in the boattailing region at $x/L = 0.91$ a stronger influence of high temperature real gas and Mach number effects than in the pressure plateau region at $x/L = 0.62$. The pressure coefficient c_{p_w} drops in all cases appreciably. Related to the $M_\infty = 10$ and $M_\infty = 10.3$ cases, the reduction of c_{p_w} at $x/L = 0.91$ is about 22 per cent (case 1.b) and 13 per cent (case 2.c).

These reductions appear not to be excessive.[32] However, considering the area of the boattailing region[33], and the distance of this region to the center-of-gravity, approximately 9.04 m, this amounts to an appreciable pitch-up mo-

[32] The reader should note, that these are values found in the lower symmetry line. They are only approximately constant in span-wise direction. Probably the effect diminishes in that direction (three-dimensionality effects due to the dihedral of the outer wing, Fig. 3.6).

[33] The boattailing region has a length of approximately 5.9 m, a width of approximately 23.0 m, hence an area of approximately 135.7 m^2.

Table 3.5. Wall pressure coefficients c_{p_w} in the lower symmetry line of the Orbiter in the boattailing region at $x/L = 0.91$ for $\alpha = 25^\circ$ (Fig. 3.38) and $\alpha = 40^\circ$ (Fig. 3.39).

Case	Fig.	α	M_∞	γ	x/L	c_{p_w}
1.a	3.38 (invisc.)	25°	10.3	1.4	0.91	0.26
1.b	3.38 (invisc.)	25°	26.1	equil.	0.91	0.20
2.a	3.39 (visc.)	40°	10	1.4	0.91	0.63
2.b	3.39 (visc.)	40°	24	1.4	0.91	0.61
2.c	3.39 (visc.)	40°	24	non-equil.	0.91	0.55

ment increment in both angle of attack cases[34], see Problem 3.5. Obviously it was mainly just this not so very large reduction of c_{p_w} in the boattailing region which caused the hypersonic pitching moment anomaly experienced with STS-1.

Remembering that the pressure coefficient at the forward stagnation point becomes larger with larger flight Mach number, and also when high temperature real gas effects are present, Fig. 3.5, we have another potential pitch-up moment increment to take into account. In this case the affected surface portion is small, maybe about 1.0 m^2, but the lever arm is rather large with approximately 21.3 m. Here, the potential increment is not large, but should be appreciated, see Problem 3.7.

3.5.3 The Forward Shift of the Center-of-Pressure

We show in a simple way that the reduction of the wall pressure in the boattailing region, Figs. 3.38 and 3.39, as well as Table 3.5, leads to a forward shift of the center of pressure and to a reduction of the normal force. Consider the action lines of the forces in Fig. 3.42. The action line of the force on the boattailing region, F_{bt}, crosses that of the force F_{ms} of the remaining portion (main surface) of the windward side of the vehicle, in the upper part of the figure. The action line a_{res} of the resulting force, F_{res}, crosses the vehicle surface in the center of pressure at x_{cp}. If now F_{bt} is reduced, then F_{res} is reduced to F'_{res}, and the new action line a'_{res} as well as the new center of pressure x'_{cp} are shifted forward. An increase of the pressure in the boattailing region would shift the center of pressure in downstream direction.

[34] The identification of this effect on the Russian BURAN vehicle (first and only flight on November 15, 1988) obviously was achieved already in 1980, before the first Space Shuttle Orbiter re-entry flight in April 1981 [50].

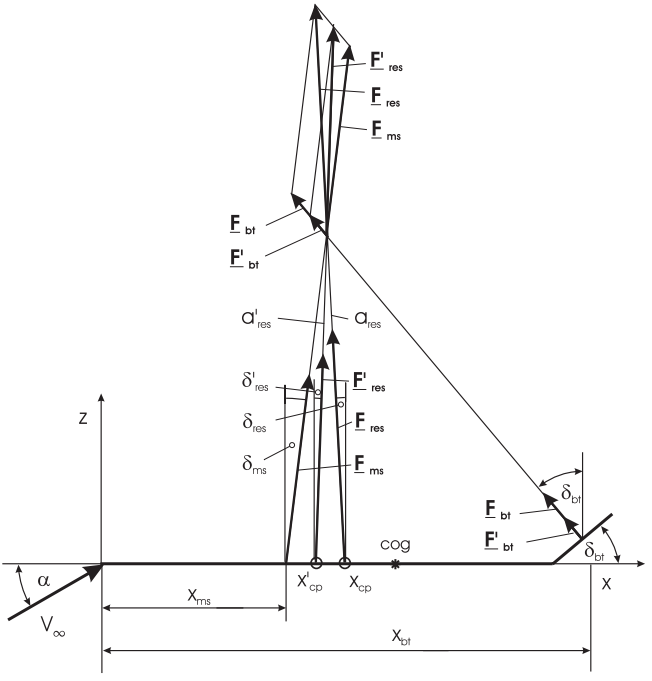

Fig. 3.42. Geometrical RHPM approximation of the windward side of the Space Shuttle Orbiter: aerodynamic forces, their action lines, and the centers of pressure. Note that the boattailing angle is exaggerated.

If the boattailing angle δ_{bt} and all other angles δ are very small,[35] we can write the simple balance

$$x_{cp}\, F_{res} = x_{ms}\, F_{ms} + x_{bt}\, F_{bt}, \tag{3.10}$$

and find with $F_{res} = F_{ms} + F_{bt}$ for x_{cp}

$$x_{cp} = \frac{x_{ms} + x_{bt}(F_{bt}/F_{ms})}{1 + F_{bt}/F_{ms}}. \tag{3.11}$$

If $F_{bt} \leqq F_{ms}$ we get

$$x_{cp} \approx \left(x_{ms} + x_{bt}\frac{F_{bt}}{F_{ms}}\right)\left(1 - \frac{F_{bt}}{F_{ms}}\right), \tag{3.12}$$

and finally

$$x_{cp} \approx x_{ms} + (x_{bt} - x_{ms})(F_{bt}/F_{ms}). \tag{3.13}$$

This relation reflects directly the observation which we made with the help of Fig. 3.42, viz., the reduction of the wall pressure in the boattailing region and

[35] In this case, the resultant force is equal to the normal force: $F_{res} = N$.

hence of F_{bt} results in a forward shift of the center of pressure. The pitch-up moment is increased, the normal force reduced, the other forces (axial, lift, drag) are, due to the given configuration and flight attitude, only a little changed.

Problem 3.8 yields despite the simple approach for $\alpha = 40°$ a forward shift of approximately 0.3 m which compares well with the data given in [14]. The original data were: center-of-gravity located at $x_{cog} = 21.30$ m ($x_{cog}/L_{ref} = 0.65$), center of pressure at $x_{cp} \approx 21.71$ m. This means $x_{cp} > x_{cog}$ and a positive static stability margin, Sub-Section 3.4.2. Even with the forward shift of $|\Delta x_{cp}| \approx 0.3$ m the margin would remain positive.

However, the actually flown center-of-gravity was $0.667 \lessapprox x_{cog}/L_{ref} \lessapprox 0.671$ [21], which amounts to $x_{cog} = 21.86$–21.99 m. The stability margin was negative from the beginning. The predicted downward deflection of the body flap as the main trim surface was at high flight Mach numbers $\eta_{bf} \approx 7°$, Fig. 3.36. The (unexpected) forward shift $|\Delta x_{cp}| \approx 0.3$ m then made $\eta_{bf} \approx 17°$ necessary in flight. (Note that most of these numbers are not measured, but post-flight computed numbers.)

3.6 The Hypersonic Pitching Moment Anomaly in View of Oswatitsch's Mach Number Independence Principle

3.6.1 Introduction

When the Orbiter was developed, the major aerodynamic design tools were approximate (impact) methods and ground simulation facilities. The discrete numerical methods of aerothermodynamics were in their infancy [49]. What were available and used thoroughly were similarity rules, correlations and parameters [58]. Considered were weak and strong viscous interaction, rarefaction effects, high temperature real gas effects, etc. Also employed was, usually not explicitly mentioned, Oswatitsch's Mach number independence principle for blunt bodies in hypersonic flow [59], see also [1].

The Mach number independence principle says, basically, that above a certain flight Mach number, several properties of the flow field in the shock layer become independent.[36] of the flight Mach number[37] This principle holds for the shape of the bow shock surface, streamline patterns, the sonic surface, and the Mach lines in the supersonic part of the flow field. The density ratio ρ/ρ_∞, the pressure coefficient c_p and with the latter the force and moment coefficients, are also independent of M_∞. These items thus do not depend on the free-stream or flight Mach number, but only on the body shape and also on the ratio of specific heats γ. The latter means, that gas flow with constant γ must be present everywhere for Mach number independence.

[36] Independence is reached asymptotically, see for instance the graphs in Section 3.2. Independence hence has an approximative character. For certain applications it may be appropriate to define an error bound.

[37] Actually this is a precise definition of hypersonic flow.

In practice Mach number independence means that if we obtain for, a given body shape experimentally for instance the force coefficients at a large enough Mach number M'_∞ (saturation Mach number), these coefficients are valid then for all larger Mach numbers $M_\infty > M'_\infty$. This can happen, depending on the body shape, for free-stream Mach numbers as low as $M_\infty = 4$–5. In [58], it is argued, without going in detail, that Oswatitsch's independence principle for blunt bodies also holds for non-perfect gas flow and also for viscous flow.

The independence principle, although seldom cited in the literature, was underlying in the aerodynamic shape definition and the data set generation work for the Orbiter. The baseline Mach number range in ground facility simulation for the data set generation was $M \approx 8$–10, [46]. In this Mach number range the available facilities are large enough for high fidelity models while having high productivity.

Due to the thorough and risk-conscious work in the aerothermodynamic design process, the aerodynamic performance of the Orbiter was largely found as predicted. The only very critical misprediction was that of the pitching moment which, as we have seen in the last sub-section, can be traced back mostly to the flow behavior in the boattailing region.

That the blunt body Mach number independence principle holds for perfect gas flow is a matter of fact, see also the simple examples in Section 3.2. In view of the practical application, two questions arise:

1. What is (for perfect gas flow) the saturation Mach number M'_∞ for a given blunt body shape?
2. How do high temperature real gas effects affect the principle?

The first of these questions can only be answered experimentally or computationally by trial and error, taking into account that Mach number independence is reached asymptotically. The second question, whose answer can give us a clue as to why the pitching moment anomaly exist could also be approached by trial and error. In the following sub-sections we try, however, to answer the question with inviscid flow data found by computational and analytical means.

We study the influence of the flight Mach number and high temperature real gas effects on the wall pressure for the two angles of attack $\alpha = 25°$ (Fig. 3.38) and $\alpha = 40°$ (Fig. 3.39) with blunt-cone approximations, Section 10.1, of the lower symmetry line of the Space Shuttle Orbiter. The two geometries with boattailing are shown in Fig. 3.43. The generatrices of the blunted cones are the lower side symmetry lines of the Orbiter. The forward stagnation points are located at $x = 0$. The nose radii were taken from [60], see also [61], where they were introduced as effective nose radii, depending on the angle of attack. The semi-vertex angles are identical with the angles of attack. The locations X at the lower side symmetry line of the Orbiter, Fig. 3.40, are found with $x_{bc} = X/\cos\alpha$. The location $x/L = 0.82$, where the 6° boattailing, Sub-Section 3.5.2, begins, are $x_{bc} = 24.35$ m and 20.58 m, respectively.

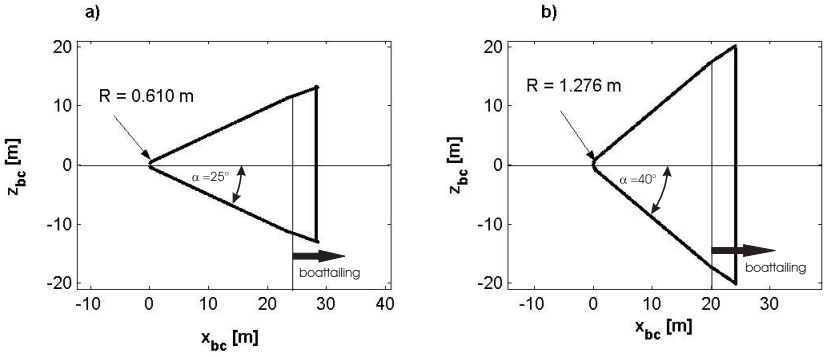

Fig. 3.43. Blunt cone approximation of the lower symmetry line of the Space Shuttle Orbiter for two angles of attack: a) $\alpha = 25°$, b) $\alpha = 40°$. The semi-vertex angles of the blunt cones are identical with the angles of attack.

3.6.2 Wall Pressure Coefficient Distribution

The wall pressure coefficient $c_{p_w}(x)$ was found with a time marching finite-difference method for the solution of the non-conservative Euler equations with bow shock fitting [62]. This method gives an accurate bow shock location and excellent entropy conservation along streamlines, particularly along the body surface. An advanced shock fitting method based on the quasi-conservatively formulated Euler equations [63], was employed for the determination of the data given in Fig. 3.44 [64].

Figure 3.44 shows the computed wall pressure coefficients for four flight Mach numbers for perfect (ID) and equilibrium (EQ) real gas for the blunt cone approximations of the windward symmetry line of the Space Shuttle Orbiter at the two angles of attack. Note that the distributions are given along the generatrices of the blunt-cone configurations, Fig. 3.43, i.e., on the real windward symmetry line of the Orbiter, Fig. 3.40. The results are in good qualitative and quantitative agreement with the data of Figs. 3.38 and 3.39.

In the boattailing region, however, we see a different qualitative behavior compared to Figs. 3.38 and 3.39. Here, we reach $c_{p_w}(x)$ plateaus, which is not the case there. This difference is caused by the geometrical modeling of the onset of the boattailing at the blunt cones, which is different from that at the Orbiter. In general, ahead of the boattailing region, the influence of M_∞ and high temperature real gas effects is small for both angles of attack. Although the curves are not very smooth, we see that $c_{p_w}(x)$ is slightly smaller for larger M_∞ and in the equilibrium, real gas case compared to the perfect gas case. The picture changes in the boattailing region. Here, the influence of M_∞ is still small, but the real gas effect is strong. All is more pronounced in the 40° cases.

To gain more insight, we investigate now parametrically with the method [62] the influence of flight Mach number M_∞ and high temperature real gas

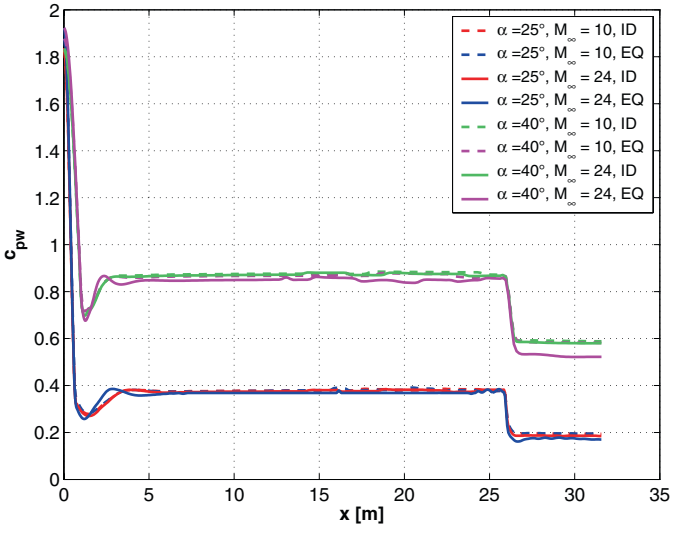

Fig. 3.44. Space Shuttle Orbiter windward symmetry line (blunt cone approximation) with boattailing: $c_{p_w}(x)$ for four flight Mach numbers M_∞, inviscid flow, $\alpha = 25°$, $\alpha = 40°$ [64]. ID: perfect gas, EQ: equilibrium real gas.

effects, the latter in terms of the effective ratio of specific heats γ_{eff}, on $c_{p_w}(x)$. We again apply the blunt cone approximation to the Orbiter windward side and also include a case without boattailing.

First, we examine the pressure-coefficient distributions of the configuration without boattailing for four flight Mach numbers M_∞ and with a perfect gas. In Fig. 3.45, we see for both the $\alpha = 25°$ and $40°$ cases for the three larger flight Mach numbers good qualitative and quantitative agreement with the c_{p_w} distributions in Figs. 3.38 and 3.39. In the region, where boattailing is not present, the pressure coefficient remains the same as upstream of it. The difference of the $M_\infty = 3.5$ curve to the curves of the other flight Mach numbers is somewhat larger for the $\alpha = 40°$ case than for the $\alpha = 25°$ case. Mach number independence is present for the larger Mach numbers, however M'_∞ was not determined. The pressure coefficients decrease only very slightly. The crossover region is not discernible. We note the typical small undershoot under the plateau pressure ahead of the plateau and little kinks due to the curvature jump at the junction of the blunt nose and the cone. Next we study results for the configuration with boattailing. In the boattailing region we now observe a spreading of the $c_{p_w}(x)$ curves. This spreading is very small for the $\alpha = 25°$ case and a little larger for the $\alpha = 40°$ case, Fig. 3.46. Any differences become negligibly small once Mach number independence is reached.

Before we examine high temperature real gas effects, we look at aspects of the Mach number independence principle different from the $c_{p_w}(x)$ behavior. We have mentioned that the independence also pertains to the shape of the bow

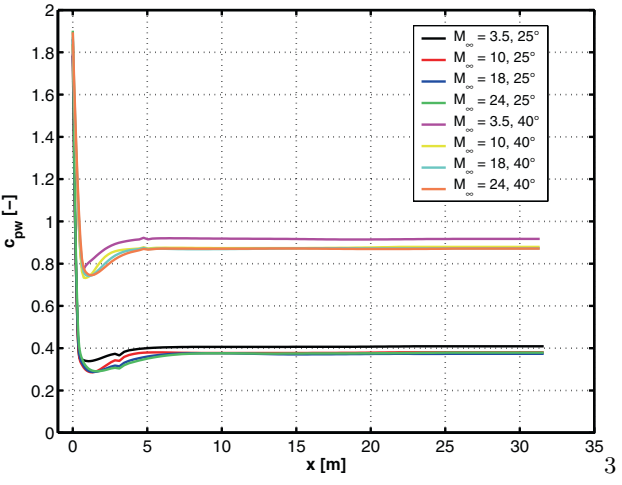

Fig. 3.45. Space Shuttle Orbiter windward symmetry line (blunt cone approximation) *without* boattailing: $c_{p_w}(x)$ for four flight Mach numbers, inviscid flow, perfect gas, $\alpha = 25°$ and $40°$.

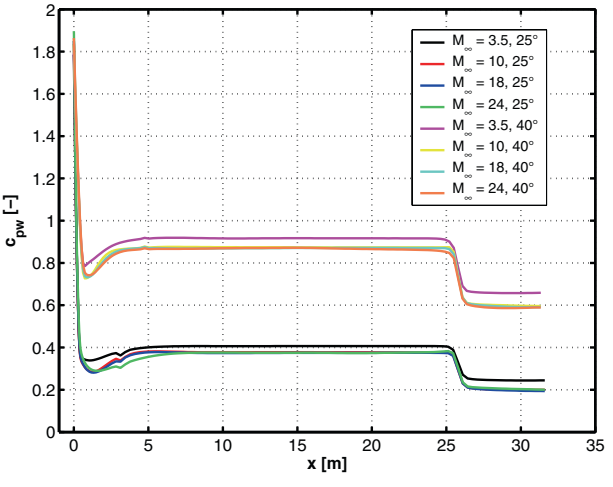

Fig. 3.46. Space Shuttle Orbiter windward symmetry line (blunt cone approximation) *with* boattailing: $c_{p_w}(x)$ for four flight Mach numbers, inviscid flow, perfect gas, $\alpha = 25°$ and $\alpha = 40°$.

shock surface, the pattern of the streamlines, etc. In the following three figures, we show for the Space Shuttle Orbiter windward symmetry plane in the blunt cone approximation the traces of the bow shock surface and c_p contours. The angle of attack in all cases is $\alpha = 40°$. The flight Mach numbers are $M_\infty = 3.5$, Fig. 3.47, $M_\infty = 10$, Fig. 3.48, and $M_\infty = 24$, Fig. 3.49. The contours in the enlargements of the figures begin each with $c_p = 0.8$ to the right, then we

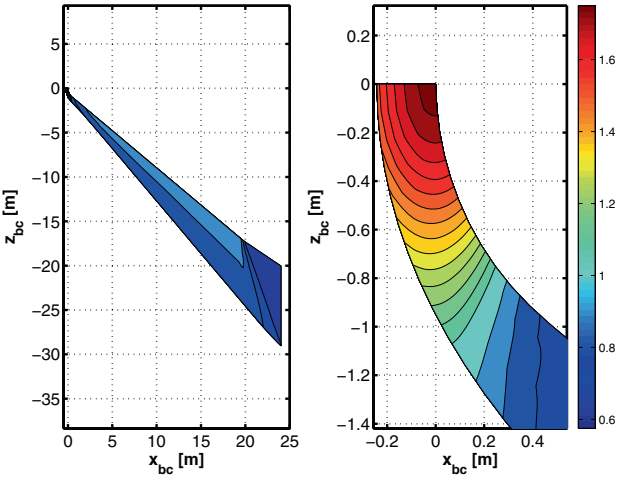

Fig. 3.47. Space Shuttle Orbiter windward symmetry plane (blunt cone approximation) *without* boattailing: $M_\infty = 3.5$, $\alpha = 40^\circ$, bow shock shape and iso-c_p lines, inviscid flow, perfect gas.

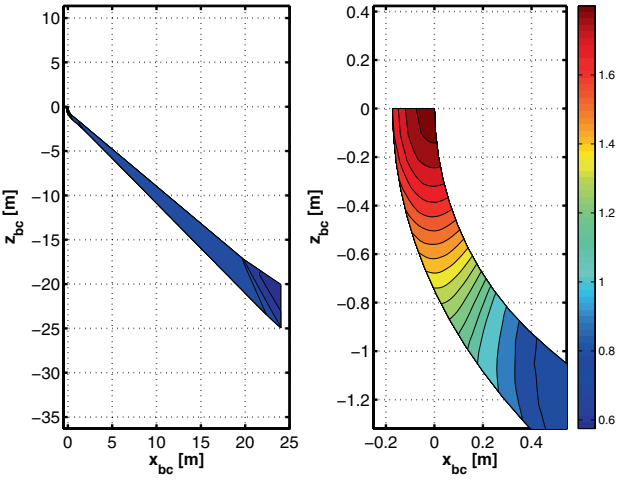

Fig. 3.48. Space Shuttle Orbiter windward symmetry plane (blunt cone approximation) *with* boattailing: $M_\infty = 10$, $\alpha = 40^\circ$, bow shock shape and c_p contours, inviscid flow, perfect gas.

have three times the increment $\Delta c_p = 0.1$, and beginning with $c_p = 1.1$ the increment is $\Delta c_p = 0.05$.

We observe first that the bow shock lies close to the body surface for all three Mach numbers, being even closer at higher Mach numbers. For the latter the bow shock shapes are virtually identical, except for the boattailing area. In the boattailing area, for $M_\infty = 24$, a slightly stronger expansion is indicated than for $M_\infty = 10$, which is also weakly seen in Fig. 3.46. Very small differences are also present in the stagnation point region.

The effective Mach number independence for the two larger Mach numbers is also evident from the pressure coefficient contours. In the stagnation point region, we see small differences, see also Fig. 3.5. We note that, in general, Mach number independence, if present, appears to be more evident somewhat away from the stagnation point area—downstream of the crossover point—in the presumably existing benign wall Mach number interval, Sub-Sections 3.2.1 and 3.6.3. This is indicated by the data in Table 3.6. At the stagnation point, in terms of the Orbiter geometry $x/L = 0$, we find a $\Delta c_p = +0.031$ from $M_\infty = 10$ to $M_\infty = 24$. At $x/L = 0.62$, we find $\Delta c_{p_w} = -0.006$ (compare with Table 3.4). Finally in the middle of the boattailing region $x/L = 0.91$, $\Delta c_{p_w} = -0.017$ (compare with Table 3.5). The data at the two latter points illustrate the crossover of the c_{p_w} curves.

Let us now examine the influence of high temperature real gas effects. They are studied for the $\alpha = 25°$ and the $\alpha = 40°$ case for $M_\infty = 10$ with the help of three γ_{eff}. The $c_{p_w}(x)$ distributions in Fig. 3.50 for the configuration with-

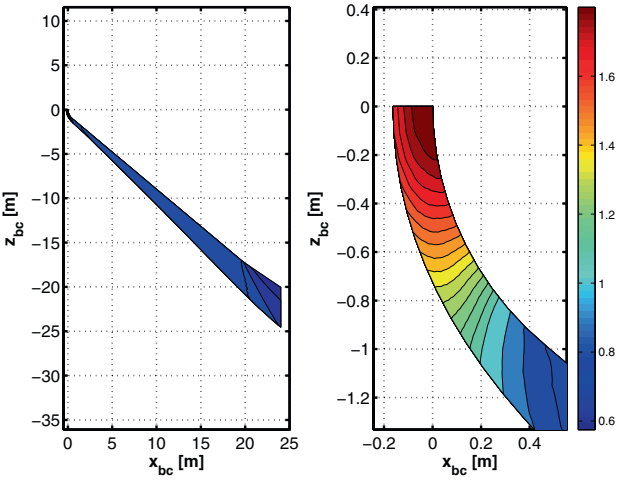

Fig. 3.49. Space Shuttle Orbiter windward symmetry plane (blunt cone approximation) *with* boattailing: $M_\infty = 24$, $\alpha = 40°$, bow shock shape and c_p contours, inviscid flow, perfect gas.

Table 3.6. Space Shuttle Orbiter windward symmetry line (blunt cone approximation) *with* boattailing: c_{p_w} at three locations x_{bc} (blunt cone), x/L (Orbiter), $\alpha = 40°$, inviscid flow, perfect gas.

x_{bc} [m]	x/L [−]	$c_{p_w}\|_{M_\infty=3.5}$	$c_{p_w}\|_{M_\infty=10}$	$c_{p_w}\|_{M_\infty=24}$
0.0	0	1.790	1.833	1.864
14.37	0.62	0.917	0.873	0.867
21.09	0.91	0.659	0.607	0.590

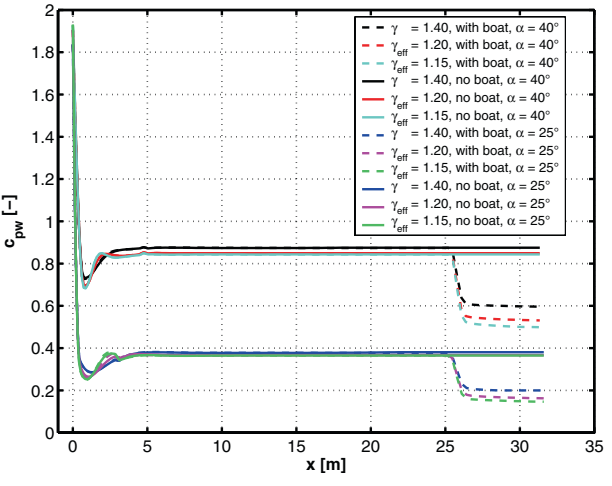

Fig. 3.50. Space Shuttle Orbiter windward symmetry line (blunt cone approximation) *without* and *with* boattailing: $c_{p_w}(x)$ for $M_\infty = 10$, and three different γ_{eff}, inviscid flow, $\alpha = 25°$ and $\alpha = 40°$.

out boattailing show very little influence of γ_{eff} for $\alpha = 25°$, and somewhat more for $\alpha = 40°$. The pressure coefficient decreases slightly in any case with decreasing γ_{eff}.

For the configuration with boattailing, we see in the boattailing region the spreading of the c_{p_w} curves similar to that we have seen for different Mach numbers M_∞, Fig. 3.46, but much stronger. The spreading is also stronger for $40°$ than for $\alpha = 25°$. In any case we observe quantitatively the same behavior as seen in Figs. 3.38 and 3.39.

These parametric studies, performed for the $\alpha = 25°$ and the $\alpha = 40°$ case, and with γ_{eff} only for $M_\infty = 10$, show for large flight Mach numbers in the boattailing region high temperature real gas effects having a strong effect on $c_{p_w}(x)$, which is much stronger than that of the flight Mach number. For the

configuration without boattailing, neither of the two effects have an appreciable influence on $c_{p_w}(x)$.

3.6.3 A Simple Analysis of Flight Mach Number and High-Temperature Real Gas Effects

With Oswatitsch's Mach number independence principle for blunt bodies in the background, we now investigate the expansion history at the lower symmetry line of the flight vehicle with the help of a simple analysis, assuming one-dimensional inviscid flow. We relate the wall pressure coefficient c_{p_w} with the Mach number of the inviscid flow at the wall (boundary-layer edge) M_w, using M_∞, $\gamma_{\inf}$, and γ_{eff} across the bow shock and along the body surface as parameters. The limitation is that we can do this only for planar flow and not, as needed in our case, for conical flow. Nevertheless, we can gain helpful insight from the analysis.

Assuming adiabatic expansion along the windward side of the vehicle (one-dimensional consideration along the lower symmetry line), beginning at the stagnation point, we find

$$\frac{p_w}{p_\infty} = \frac{p_w}{p_{t_2}} \frac{p_{t_2}}{p_\infty} = \left(1 + \frac{\gamma - 1}{2} M_w^2\right)^{-\gamma/(\gamma-1)} \frac{p_{t_2}}{p_\infty}. \tag{3.14}$$

yielding:

$$c_{p_w} = \frac{p_w - p_\infty}{q_\infty} = \frac{p_\infty}{q_\infty}\left(\frac{p_w}{p_\infty} - 1\right) = \frac{2}{\gamma_\infty M_\infty^2}\left(\frac{p_w}{p_\infty} - 1\right). \tag{3.15}$$

We assume that the forward stagnation point streamline crosses the normal-shock portion of the bow shock and find p_{t_2} for the chosen γ_{eff} from the relations in Sub-Section 10.1.3. We choose two free-stream Mach numbers close to those in Figs. 3.38 and 3.39, viz., $M_\infty = 10$ and 24, and include $M_\infty \to \infty$.

For each Mach number, we choose four $\gamma_{eff} = 1.1$, 1.2, 1.3 and 1.4. These values are based on [55] where $\gamma_{eff} \approx 1.3$ just behind the bow shock in the nose region, $\gamma_{eff} \approx 1.12$ close to the body in the nose region, and $\gamma_{eff} \approx 1.14$ along the lower body surface. The Mach number interval chosen is $0 \leqq M_w \leqq 5$ where $M_w = 0$ represents the stagnation point and $M_w = 1$, of course, is the sonic point at the wall. In Fig. 3.51. we show computed wall pressure coefficients for $M_\infty = 24$ and the four chosen γ_{eff}. The c_{p_w} curves drop from their maxima in the stagnation point monotonically with increasing M_w. At the stagnation point, we see the behavior shown in Fig. 3.5, viz., the stagnation pressure coefficient increases with decreasing γ_{eff}.

Remember, however, the remark above, that these data are not quantitatively representative for the Space Shuttle Orbiter. In [49], results from γ_{eff} studies for a blunt 30° cone are given, unfortunately without the wall Mach number. They also show the crossover of the c_{p_w} curves, which happens in

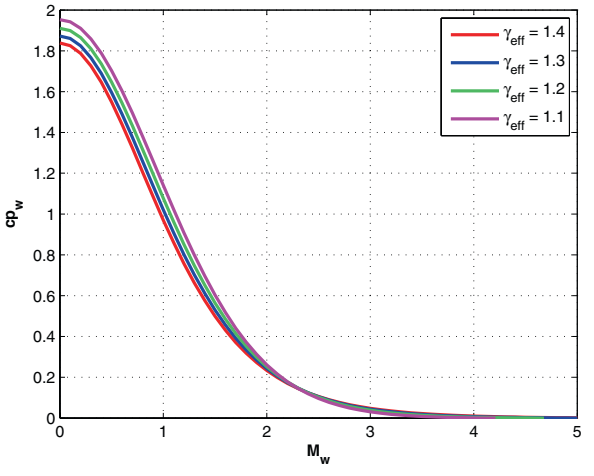

Fig. 3.51. Wall pressure coefficient c_{p_w} as function of wall Mach numbers M_w for $M_\infty = 24$ and four values of γ_{eff}.

Fig. 3.51 at $M_w \approx 2.2$. At the stagnation point, the curves for the smallest γ_{eff} are above and then switch places with the curves for the larger values.

In order to get a better impression of the differences between the different results, we consider $c^\star_{p_w}$, the wall pressure coefficients normalized by values at $M_\infty \to \infty$ and $\gamma = 1.4$. In this way, we can visualize the increments which exist in view of the Mach number independence principle. The results in Fig. 3.52 show that ahead of the crossover region, i.e., for $M_w \lessapprox 2.2$, the differences $\triangle c^\star_{p_w} = c^\star_{p_w} - 1$ between the different results and the ones for $M_\infty \to \infty$, $\gamma = 1.4$ are bounded and relatively small. The influence of M_∞ is smaller in general than that of γ_{eff}. For $M_w \gtrapprox 2.2$, the differences are unbounded and become large with increasing M_w. The difference is more for smaller γ_{eff}.

The above results apply for the planar case. Results for the blunt cone case in Sub-Section 3.6.2, more relevant for the Orbiter, exhibit exactly the same properties, however, with much smaller $\triangle c^\star_{p_w}$. Unfortunately, we have no M_w results available belonging to the c_{p_w} results of Sub-Section 3.6.2. Initial results show for the $\alpha = 40°$ case a wall Mach number rise from levels of $M_w \approx 1.2$ ahead of the boattailing to ≈ 1.5 in the boattailing region. Data for the $\alpha = 25°$ case are not consistent. For a perfect gas and the given boattailing angle of 6°, we find with the data of the Prandtl–Meyer expansion [65], at small wall Mach numbers a $\Delta M_w \approx 0.2$. A dependence of $c^\star_{p_w}$ on the angle of attack and on one or more other parameters may be possible. In any case, it appears that the crossover region lies at wall Mach numbers smaller than $M_w \lessapprox 2.2$.

However, the general results of this sub-section and of Sub-Section 3.6.2 indicate, like the data in Figs. 3.38 and 3.39, that a benign wall Mach number interval exists, where the Mach number independence principle is valid despite the presence of high temperature real gas effects. In other words: *If for a given*

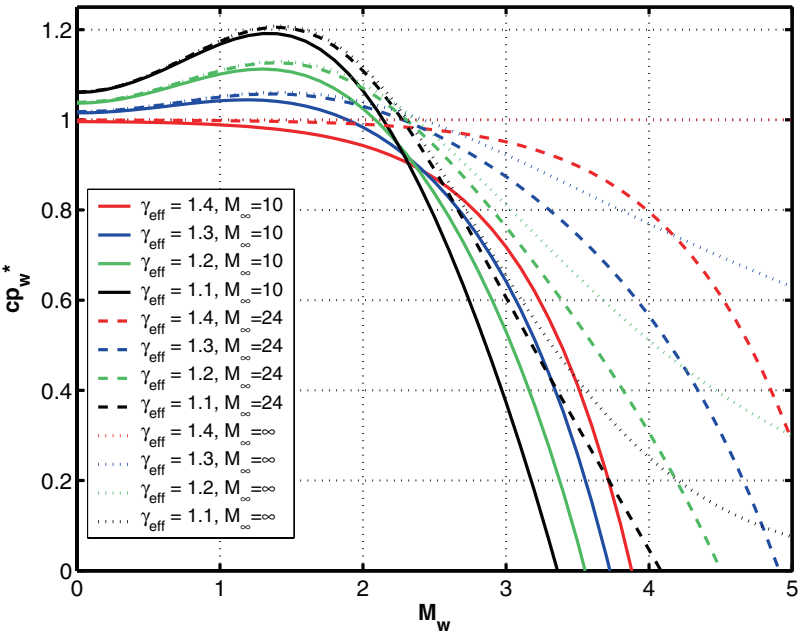

Fig. 3.52. Normalized wall pressure coefficient $c^{\star}_{p_w}$ as function of wall Mach numbers M_w for selected pairs of M_∞ and γ_{eff}.

body shape and a given flight Mach number interval (flight) Mach number independence exists, presumably a benign wall (boundary-layer edge) Mach number interval is present where independence from high temperature real gas effects also exists. A quantification of the interval would be desirable.

3.6.4 Reconsideration of the Pitching Moment Anomaly and Summary of Results

In the preceding sub-sections, the inviscid blunt-cone flow field in terms of c_{p_w} along the symmetry line of the windward side of the Orbiter was studied as well as the inviscid flow expansion history of planar one-dimensional flow. The γ_{eff} approach was employed in the latter in order to account for high temperature real gas effects. No viscous effects, neither weak nor strong interaction, and also no low density effects were taken into account, assuming that they play only a minor role.

The Orbiter windward side is largely flat. However, the dominant flow features are governed by the vehicle shape approximately up to the canopy location, which can be considered as a blunt cone. Where the lower side is approximately flat, the flow properties along the windward centerline are to a good approximation the same also in lateral direction (quasi two-dimensional distribution, Sub-Section 3.2.2).

If we accept the limitations of our investigations, and flight Mach number independence in Oswatitsch's sense is given, the general results are the following:

1. Flight Mach number *and* high temperature real gas effects, defined as deviations from the $M_\infty \to \infty$, $\gamma = 1.4$, are smallest in a certain low wall Mach number interval. If—in the case of the Orbiter—at the pressure coefficient plateau, present at $0.4 \lessapprox x/L \lessapprox 0.82$, M_w lies in this presumably existing benign interval, Oswatitsch's Mach number independence principle is only weakly violated.[38] *Without boattailing, C_N and C_M would only be slightly affected because the lower vehicle surface is predominantly exposed to this wall Mach number interval, i.e., the wall Mach number plateau lies in the benign wall Mach number interval.* This holds for a large angle of attack interval, as is well indicated in Figs. 3.38 and 3.39. *A RV-W with these flow properties on the lower side and, in any case, without boattailing thus will be insensitive with regard to flight Mach number and high temperature real gas effects.*
2. Boattailing leads to a supersonic expansion, provided that M_w at the pressure plateau is supersonic. This is given in the case of the Orbiter at both the angles of attack $\alpha = 25°$ and $40°$, Figs. 3.38 and 3.39. *If now M_w increases sufficiently, the—yet exactly to be defined—benign wall Mach number interval is left. Both—dominating—high-temperature real gas effects and—weaker—flight Mach number effects come to influence, Figs. 3.38 and 3.39. This is the cause of the pitching moment anomaly of the Orbiter, as was conjectured earlier by several authors.* Even if the effect is small, the large affected surface portion at the windward side leads to the adverse increment of the pitching moment, see the discussion at the end of Sub-Section 3.5.2. A small role is also played by the forward stagnation point region.
3. Boattailing leads to a subsonic compression, if M_w at the pressure plateau is subsonic. In the case of the Orbiter at $\alpha = 40°$ the wall Mach number at the pressure plateau is slightly supersonic. There exists a higher angle of attack, where the wall Mach number will be subsonic, and then in the boattailing region c_{p_w} (and C_N) will be increased, causing a pitch-down increment of C_M. This happens for the Orbiter at $\alpha \gtrapprox 50°$, Sub-Section 3.5.2. Our results indicate that without boattailing, this pitching moment reversal would not occur. However, our analysis is not able to give an answer to what happens, if the whole lower side of a RV-W is in the subsonic wall Mach number regime.
4. In general, boattailing for a RV-W should be avoided in view of the pitching moment sensitivities in the hypersonic flight domain. If boattailing is needed to improve configurational and low-speed flight properties or for other reasons, data uncertainties in high Mach number, ground facility

[38] Oswatitsch gives no criterion in [59] for the range of validity of his principle.

simulation must be expected. However, with the capabilities of numerical aerothermodynamics, it is now possible to identify sensitivities and uncertainties early on and to design appropriate correction schemes for the experimental data. Besides the pitching moment sensitivity of RV-W's with boattailing, other sensitivities which curtail the Mach number independence of aerodynamic properties are not known. Control surface deflections, winglets, and the lateral movement of the flight vehicle must be considered with care in this regard.

3.6.5 Concluding Remarks

The reader might be tempted to think the following. For the Space Shuttle Orbiter, because of the large amount of data needed for the aerodynamic data set, ground facility simulation has to rely on continuously running tunnels in the $M = 8$–10 domain, without a sufficiently accurate representation of high temperature real gas effects. This should be no more a problem now in view of the present numerical simulation capabilities. Such a thinking would be a mistake for two reasons:

1. There is no doubt, that results of well-defined numerical simulations can shed light on most complicated aerodynamic/aerothermodynamic design problems. Even if the discrete numerical methods of aerothermodynamics, together with flow physics and thermo-chemical models, and the still increasing power of computers allow for an accurate and reliable prediction, it is always necessary in vehicle design to understand the involved physics and the data from numerical simulations.
2. Design work involves other disciplines besides aerodynamics and aerothermodynamics. These often use their own prediction methods, if they need aerodynamic coefficients or loads. These methods are not necessarily the adequate ones. Time and cost pressures in industrial design work, in addition, lead to the use of inexpensive and fast computation methods that are not necessarily accurate enough. These problems can possibly be overcome with more holistic approaches in design work: keyword "Virtual Product", see Section 1.2 and the prologue of Chapter 8.

3.7 Problems

Problem 3.1 We consider six re-entry trajectory points of the Space Shuttle Orbiter mission STS-2, Fig. 2.2 with approximate flight Mach numbers: 1) $H = 80$ km, $M_\infty = 26.4$, 2) $H = 70$ km, $M_\infty = 22.1$, 3) $H = 60$ km, $M_\infty = 15.7$, 4) $H = 50$ km, $M_\infty = 10.3$, 5) $H = 40$ km, $M_\infty = 6.1$, 6) $H = 30$ km, $M_\infty = 3.4$.

How large are the dynamic pressures q_∞ in these points? How do they compare to the constraint given in Sub-Section 2.1.2?

Problem 3.2 Compute the total enthalpies for the six re-entry trajectory points of Problem 3.1. Determine the percentage of the kinetic part at each point.

Problem 3.3 During re-entry, the Space Shuttle Orbiter flies at $M_\infty = 26.4$ at an altitude of $H = 80$ km. The angle of attack is $\alpha = 40°$. The lift coefficient is assumed to be $C_L = 0.884$ [20], the reference area is $A_{ref} = 249.91$ m^2. We assume further a very small and and time-independent flight path angle γ.

How large is a) the re-entry mass of the Orbiter, b) the g-reduction due to the curved flight path in per cent, c) the re-entry weight of the Orbiter at sea level.

Problem 3.4 The X-38 flies at very small and time-independent flight path angle γ at 80 km altitude. We assume its mass to be $m = 8,618$ kg, the reference area is $A_{ref} = 21.67$ m^2, and the lift coefficient $C_L = 0.52$ is Mach number independent. How large is the flight Mach number M_∞?

Problem 3.5 Assume that the aerodynamic data base contains for the boattailing region the mean pressure coefficient $c_{p_{w,2.a}} = 0.63$ at $\alpha = 40°$, Table 3.5. In flight, the actual mean pressure coefficient is $c_{p_{w,2.c}} = 0.55$, Table 3.5. How large is the resulting difference of the forces acting on the boattailing surface, the delta force, if flight Mach number and altitude are $M_\infty = 24$, $H_\infty = 70$ km? How large are ΔM and ΔC_M?

The boattailing region of the Orbiter has an area of approximately $A_{bt} = 5.9$ m $\times$ 23.0 m $= 135.7$ m^2. Its mean location is at $x/L_{ref} = 0.91$. The center of gravity is assumed to be located axially at $x/L_{ref}|_{cg} = 0.65$, $L_{ref} = 32.7736$ m [14]. Neglect the z location. The reference area is $A_{ref} = 249.91$ m^2. The total plan area, Fig. 3.40, is $A_{plan} = 361.3$ m^2. The reference length for the pitching moment is the mean wing chord $\overline{c} = 12.06$ m. Neglect contributions of the axial force to the pitching moment. Assume that the delta force acts orthogonally to the x axis of the flight vehicle.

Problem 3.6 The lift and drag coefficients of the Space Shuttle Orbiter at $\alpha = 40°$ and above $M_\infty = 20$ are Mach number independent, and given by $C_L = 0.884$ and $C_D = 0.821$ [20].

a) How large are the normal and the axial force coefficient C_N and C_X? b) Compare the normal force coefficient to very simple estimates made with the help of the data in Tables 3.4 and 3.5, for the cases 2.a and 2.c. c) Discuss the results.

Problem 3.7 Around the forward stagnation point of the Space Shuttle Orbiter, we have above $M_\infty = 20$ Mach number independence for perfect gas $c_{p_{w,perfect}} \approx c_{p_{w,perfect,stag}}$ and for real gas $c_{p_{w,real,stag}} \approx 1.94$ (point No. 7 in Fig. 3.5).

The real gas, pressure coefficient leads to a pitching moment increment. At $M_\infty = 22.1$ and $H = 70$ km, how large is a) $c_{p_{w,perfect,stag}}$ and what is

the assumption, b) the increment of the normal force coefficient and c) the increment of the pitching moment coefficient. Assume that the pressures act in the normal force direction (no axial force contribution to the pitching moment) on a surface portion $\Delta A_{nose} = 1.0\ \mathrm{m}^2$ with a lever arm to the center-of-gravity of $x_l = 21.3$ m.

Problem 3.8 At $M_\infty = 22.1$ and $H = 70$ km, the Mach number independent moment coefficient is $C_M = -0.041$ and the normal force coefficient $C_N = 1.205$. The x-location of the center-of-gravity is $x_{cog} = 0.65 L_{ref}$, $L_{ref} = 32.7736$ m. The plan area is $A_{plan} = 361.3\ \mathrm{m}^2$, the boattailing area $A_{bt} = 135.7\ \mathrm{m}^2$, and the remaining main surface area $A_{ms} = 225.6\ \mathrm{m}^2$. The reference area is $A_{ref} = 249.91\ \mathrm{m}^2$, the moment reference length $\overline{c} = 12.06$ m, and the dynamic pressure $q_\infty = 1.79$ kPa. The boattailing force N_{bt} is assumed to act at $x_{bt}/L_{ref} = 0.91$, Table 3.5.

Assume that the axial force does not contribute to the pitching moment and that the forces on the main surface and on the boattailing surface act in the direction of the normal force. In the nomenclature of Fig. 3.42, $N \equiv F_{res}$ etc. Assume $F_{bt} = A_{bt} q_\infty c_{p_{w,2.a}}$ with $c_{p_{w,2.a}} = 0.63$, Table 3.5. How large are a) F_{bt}, F_{ms}, x_{cp}, x_{ms}, b) F'_{bt}, x'_{cp}, if $c_{p_{w,2.c}} = 0.55$, Table 3.5, c) the forward shift of the center of pressure Δx_{cp}?

References

1. Hirschel, E.H.: Basics of Aerothermodynamics. Progress in Astronautics and Aeronautics, AIAA, Reston, VA, vol. 204. Springer, Heidelberg (2004)
2. Hirschel, E.H.: Hypersonic Aerodynamics. In: Space Course 1993, vol. 1, pp. 2-1– 2-17. Technische Universität München, Germany (1993)
3. Sacher, P.W., Kunz, R., Staudacher, W.: The German Hypersonic Experimental Aircraft Concept. In: 2nd AIAA International Aerospaceplanes Conference, Orlando, Florida (1990)
4. Hirschel, E.H., Grallert, H., Lafon, J., Rapuc, M.: Acquisition of an Aerodynamic Data Base by Means of a Winged Experimental Reentry Vehicle. Zeitschrift für Flugwissenschaften und Weltraumforschung 16(1), pp. 15–27 (1992)
5. Abgrall, R., Desideri, J.-A., Glowinski, R., Mallet, M., Periaux, J. (eds.): Hypersonic Flows for Reentry Problems, vol. III. Springer, Berlin (1992)
6. Lyubimov, A.N., Rusanow, V.V.: Gas Flows Past Blunt Bodies. NASA TT-F-714, Part II (1973)
7. Weilmuenster, K.J., Gnoffo, P.A., Greene, F.A.: Navier–Stokes Simulations of Orbiter Aerodynamic Characteristics. In: Throckmorton, D.A. (ed.) Orbiter Experiments (OEX) Aerothermodynamics Symposium. NASA CP-3248, Part 1, pp. 447–494 (1995)
8. Edney, B.: Anomalous Heat Transfer and Pressure Distributions on Blunt Bodies at Hypersonic Speeds in the Presence of an Impinging Shock. FFA Rep. 115 (1968)

9. Brück, S., Radespiel, R.: Navier–Stokes Solutions for the Flow Around the HALIS Configuration – F4 Wind Tunnel Conditions – DLR Internal Report, IB 129 - 96/2 (1996)
10. Hartmann, G., Menne, S.: Winged Aerothermodynamic Activities. MSTP Report, H-TN-E33.3-004-DASA, DASA, München/Ottobrunn, Germany (1996)
11. Riedelbauch, S.: Aerothermodynamische Eigenschaften von Hyperschallströmungen über strahlungsadiabate Oberflächen (Aerothermodynamic Properties of Hypersonic Flows past Radiation-Cooled Surfaces). Doctoral Thesis, Technische Universität München, Germany (1991) (Also DLR-FB 91-42, 1991)
12. Weiland, C.: Synthesis of Results for Problem VII, Delta Wing. In: Abgrall, R., Desideri, J.-A., Glowinski, R., Mallet, M., Periaux, J. (eds.) Hypersonic Flows for Reentry Problems, vol. III, pp. 1014–1027. Springer, Heidelberg (1992)
13. Liepmann, H.W., Roshko, A.: Elements of Gasdynamics. Dover Publications, Mineola (2002)
14. Griffith, B.F., Maus, J.R., Best, J.T.: Explanation of the Hypersonic Longitudinal Stability Problem – Lessons Learned. In: Arrington, J.P., Jones, J.J. (eds.) Shuttle Performance: Lessons Learned. NASA CP-2283, Part 1, pp. 347–380 (1983)
15. Becker, J.V.: The X-15 Project. Astronautics and Aeronautics 2, 52–61 (1964)
16. McLellan, C.H.: A Method for Increasing the Effectiveness of Stabilizing Surfaces at High Supersonic Mach Numbers. NACA RM L54F21 (1954)
17. Arrington, J.P., Jones, J.J. (eds.): Shuttle Performance: Lessons Learned. NASA CP-2283 (1983)
18. Throckmorton, D.A. (ed.): Orbiter Experiments (OEX) Aerothermodynamics Symposium. NASA CP-3248 (1995)
19. Martin, L.: Aerodynamic Coefficient Measurements, Body Flap Efficiency and Oil Flow Visualization on an Orbiter Model at Mach 10 in the ONERA S4 Wind Tunnel. ONERA Report No. 8907 GY 400G (1995)
20. N.N.: Aerodynamic Design Data Book – Orbiter Vehicle STS-1. Rockwell International, USA (1980)
21. Iliff, K.W., Shafer, M.F.: Extraction of Stability and Control Derivatives from Orbiter Flight Data. In: Throckmorton, D.A. (ed.) Orbiter Experiments (OEX) Aerothermodynamics Symposium. NASA CP-3248, Part 1, pp. 299–344 (1995)
22. Hartmann, G., Menne, S., Schröder, W.: Uncertainties Analysis/Critical Points. HERMES Report, H-NT-1-0329-DASA, DASA, Mücheń/Ottobrunn, Germany (1994)
23. Courty, J.C., Rapuc, M., Vancamberg, P.: Aerodynamic and Thermal Data Bases. HERMES Report, H-NT-1-1206-AMD, Aviation M. Dassault, St. Cloud, France (1991)
24. N.N.: HOPE-X Data Base. Industrial communication, European Aeronautic Defence and Space Company, EADS/Japanese Space Agency, NASDA (1998)
25. Tsujimoto, T., Sakamoto, Y., Akimoto, T., Kouchiyama, J., Ishimoto, S., Aoki, T.: Aerodynamic Characteristics of HOPE-X Configuration with Twin Tails. AIAA Paper 2001-1827 (2001)
26. Pamadi, B.N., Brauckmann, G.J., Ruth, M.J., Furhmann, H.D.: Aerodynamic Characteristics, Database Development and Flight Simulation of the X-34 Vehicle. AIAA Paper 2000-0900 (2000)
27. `http://www.dfrc.nasa.gov/gallery`

28. Pamadi, B.N., Brauckmann, G.J.: Aerodynamic Characteristics and Development of the Aerodynamic Database of the X-34 Reusable Launch Vehicle. In: Proc. 1st Int. Symp. on Atmospheric Re-Entry Vehicles and Systems, Arcachon, France (1999)
29. Brauckmann, G.J.: X-34 Vehicle Aerodynamic Characteristics. J. of Spacecraft and Rockets 36(2), pp. 229–239 (1999)
30. Tarfeld, F.: Measurement of Direct Dynamic Derivatives with the Forced-Oscillation Technique on the Reentry Vehicle X-38 in Supersonic Flow. Deutsches Zentrum für Luft- und Raumfahrt DLR, TETRA Programme, TET-DLR-21-TN-3104 (2001)
31. Labbe, S.G., Perez, L.F., Fitzgerald, S., Longo, J.M.A., Molina, R., Rapuc, M.: X-38 Integrated Aero- and Aerothermodynamic Activities. Aerospace Science and Technology 3, pp. 485–493 (1999)
32. N.N.: X-38 Data Base. Industrial communication, Dassault Aviation – NASA – European Aeronautic Defence and Space Company, EADS (1999)
33. Behr, R., Weber, C.: Aerothermodynamics – Euler Computations. X-CRV Rep., HT-TN-002/2000-DASA, DASA, München/Ottobrunn, Germany (2000)
34. Aiello, M., Stojanowski, M.: X-38 CRV, S3MA Windtunnel Test Results. X-CRV Rep., DGT No. 73442, Aviation M. Dassault, St. Cloud, France (1998)
35. Weiland, C.: X-38 CRV, S4MA Windtunnel Test Results. DASA, X-CRV Report, HT-TN-001/99-DASA, DASA, München/Ottobrunn, Germany (1999)
36. Görgen, J.: CFD Analysis of X-38 Free Flight. TETRA Programme, TET-DASA-21-TN-2401, DASA, München/Ottobrunn, Germany (1999)
37. Daimler-Benz Aerospace Space Infrastructure, FESTIP System Study Proceedings. FFSC-15 Suborbital HTO-HL System Concept Family. EADS, München/Ottobrunn, Germany (1999)
38. N.N.: PHOENIX Data Base. Internal industrial communication, EADS, München/Ottobrunn, Germany (2004)
39. Häberle, J.: Einfluss heisser Oberflächen auf aerothermodynamische Flugeigenschaften von HOPPER/PHOENIX (Influence of Hot Surfaces on Aerothermodynamic Flight Properties of HOPPER/PHOENIX). Diploma Thesis, Institut für Aerodynamik und Gasdynamik, Universität Stuttgart, Germany (2004)
40. Borrelli, S., Marini, M.: The Technology Program in Aerothermodynamics for PRORA-USV. ESA-SP-487, pp. 37–48 (2002)
41. Rufolo, G.C., Roncioni, P., Marini, M., Votta, R., Palazzo, S.: Experimental and Numerical Aerodynamic Integration and Aerodatabase Development for the PRORA-USV-FTB-1 Reusable Vehicle. AIAA Paper 2006-8031 (2006)
42. Behr, R.: CFD Computations. Private communications, EADS, München/ Ottobrunn, Germany (2007)
43. Trella, M.: Introduction to the Hypersonic Phenomena of HERMES. In: Bertin, J.J., Glowinski, R., Periaux, J. (eds.) Hypersonics. Defining the Hypersonic Environment, vol. 1, pp. 67–91. Birkhäuser, Boston (1989)
44. Etkin, B., Reid, L.D.: Dynamics of Flight Mechanics: Performance, Stability and Control. John Wiley & Sons, New York (2000)
45. Hoey, R.G.: AFFTC Overview of Orbiter-Reentry Flight-Test Results. In: Arrington, J.P., Jones, J.J. (eds.) Shuttle Performance: Lessons Learned. NASA CP-2283, Part 2, pp. 1303–1334 (1983)
46. Woods, W.C., Watson, R.D.: Shuttle Orbiter Aerodynamics – Comparison Between Hypersonic Ground-Facility Results and STS-1 Flight-Derived Results.

In: Throckmorton, D.A. (ed.) Orbiter Experiments (OEX) Aerothermodynamics Symposium. NASA CP-3248, Part 1, pp. 371–409 (1995)
47. Williams, S.D.: Columbia, the First Five Flights Entry Heating Data Series, an Overview, vol. 1, NASA CR-171 820 (1984)
48. Romere, P.O.: Orbiter (Pre STS-1) Aerodynamic Design Data Book Development and Methodology. In: Throckmorton, D.A. (ed.) Orbiter Experiments (OEX) Aerothermodynamics Symposium. NASA CP-3248, Part 1, pp. 249–280 (1995)
49. Woods, W.C., Arrington, J.P., Hamilton II, H.H.: A Review of Preflight Estimates of Real Gas Effects on Space Shuttle Aerodynamic Characteristics. In: Arrington, J.P., Jones, J.J. (eds.) Shuttle Performance: Lessons Learned. NASA CP-2283, Part 1, pp. 309–346 (1983)
50. Neyland, V.Y.: Air Dissociation Effects on Aerodynamic Characteristics of an Aerospace Plane. Journal of Aircraft 30(4), pp. 547–549 (1993)
51. Weilmuenster, K.J., Gnoffo, P.A., Greene, F.A.: Navier–Stokes Simulations of Orbiter Aerodynamic Characteristics Including Pitch Trim and Bodyflap. Journal of Spacecraft and Rockets 31(5), pp. 355–366 (1994)
52. Paulson Jr., J.W., Brauckmann, G.J.: Recent Ground-Facility Simulations of Space Shuttle Orbiter Aerodynamics. In: Throckmorton, D.A. (ed.) Orbiter Experiments (OEX) Aerothermodynamics Symposium. NASA CP-3248, Part 1, pp. 411–445 (1995)
53. Prabhu, D.K., Papadopoulos, P.E., Davies, C.B., Wright, M.J.B., McDaniel, R.D., Venkatapathy, E., Wercinski, P.F.: Shuttle Orbiter Contingency Abort Aerodynamics, II: Real-Gas Effects and High Angles of Attack. AIAA Paper 2003-1248 (2003)
54. Koppenwallner, G.: Low Reynolds Number Influence on Aerodynamic Performance of Hypersonic Vehicles. AGARD-CP-428, pp. 11-1–11-14 (1987)
55. Brauckmann, G.J., Paulson Jr., J.W., Weilmuenster, K.J.: Experimental and Computational Analysis of Shuttle Orbiter Hypersonic Trim Anomaly. Journal of Spacecraft and Rockets 32(5), pp. 758–764 (1995)
56. Goodrich, W.D., Derry, S.M., Bertin, J.J.: Shuttle Orbiter Boundary-Layer Transition: A Comparison of Flight and Wind-Tunnel Data. AIAA Paper 83-0485 (1983)
57. Boeing, Human Space Flight and Exploration, Huntington Beach, CA. Operational Aerodynamic Data Book. Boeing Document STS85-0118 CHG 9 (2000)
58. Hayes, W.D., Probstein, R.F.: Hypersonic Flow Theory. Inviscid Flows, vol. 1. Academic Press, New York (1966)
59. Oswatitsch, K.: Ähnlichkeitsgesetze für Hyperschallströmung. ZAMP II, pp. 249–264 (1951); Similarity Laws for Hypersonic Flow. Royal Institute of Technology, Stockholm, Sweden, KTH-AERO TN 16 (1950)
60. Wüthrich, S., Sawley, M.L., Perruchoud, G.: The Coupled Euler/ Boundary-Layer Method as a Design Tool for Hypersonic Re-Entry Vehicles. Zeitschrift für Flugwissenschaften und Weltraumforschung 20(3), pp. 137–144 (1996)
61. Adams, J.C., Martindale, W.R., Mayne, A.W., Marchand, E.O.: Real Gas Scale Effects on Hypersonic Laminar Boundary-Layer Parameters Including Effects of Entropy-Layer Swallowing. AIAA Paper 76-358 (1976)
62. Weiland, C.: Zwei- und dreidimensionale Umströmungen stumpfer Körper unter Berücksichtigung schallnaher Überschallströmungen. Zeitschrift für Flugwissenschaften und Weltraumforschung (ZFW) 24(3), 237–245 (1976); Translation:

Two and Three-Dimensional Flows Past Blunt Bodies with Special Regard of Supersonic Flow Close to M = 1. NASA TTF-17406 (1977)
63. Pfitzner, M., Weiland, C.: 3-D Euler Solutions for Hypersonic Mach Numbers. AGARD-CP-428, pp. 22-1–22-14 (1987)
64. Kliche, D.: Personal communication. München, Germany (2008)
65. Ames Research Staff. Equations, Tables, and Charts for Compressible Flow. NACA R-1135 (1953)